Topical Review

High-T_c SQUID biomagnetometers

M I Faley[1] , **J Dammers**[2] , **Y V Maslennikov**[3], **J F Schneiderman**[4] ,
D Winkler[5] , **V P Koshelets**[3] , **N J Shah**[2] and **R E Dunin-Borkowski**[1]

[1] Peter Grünberg Institute, Forschungszentrum Jülich GmbH, D-52425 Jülich, Germany
[2] Institute of Neurosciences and Medicine, Forschungszentrum Jülich GmbH, D-52425 Jülich, Germany
[3] The Kotel'nikov Institute of Radio Engineering & Electronics RAS, 125009 Moscow, Russia
[4] The University of Gothenburg, Institute of Neuroscience and Physiology and MedTech West, Röda stråket 10B, Sahlgrenska University Hospital, SE-413 45 Gothenburg, Sweden
[5] Department of Microtechnology and Nanoscience—MC2, Chalmers Univf5=ˆtexttx);ersity of Technology, Kemivägen 9, SE-412 96 Gothenburg, Sweden

E-mail: m.faley@fz-juelich.de

CrossMark

Abstract

In this paper, we review the preparation technology, integration in measurement systems and tests of high-T_c superconducting quantum interference devices (SQUIDs) intended for biomagnetic applications. A focus is on developments specific to Forschungszentrum Jülich GmbH, Chalmers University of Technology, MedTech West, and the University of Gothenburg, while placing these results in the perspective of those achieved elsewhere. Sensor fabrication, including the deposition and structuring of epitaxial oxide heterostructures, materials for substrates, epitaxial bilayer buffers, bicrystal and step-edge Josephson junctions, and multilayer flux transformers are detailed. The properties of the epitaxial multilayer high-T_c direct current SQUID sensors, including their integration in measurement systems with special electronics and liquid nitrogen cryostats, are presented in the context of biomagnetic recording. Applications that include magnetic nanoparticle based molecular diagnostics, magnetocardiography, and magnetoencephalography are presented as showcases of high-T_c biomagnetic systems. We conclude by outlining future challenges.

Keywords: epitaxial heterostructures, high-T_c Josephson junctions, SQUIDs, biomagnetic measurement systems, magnetocardiography, magnetoencephalography, magnetic nanoparticles

(Some figures may appear in colour only in the online journal)

1. Introduction

The field of biomagnetism encompasses the detection of extremely weak magnetic fields generated by biological systems, e.g., by ion currents in nerve cells and heart tissue or by magnetic nanoparticles (MNPs) of magnetite (Fe_3O_4) that occur naturally in living organisms due to biomineralization or are used as a contrast agent for protein assays. Several

applications of biomagnetism are relevant for non-invasive medical diagnostics, including the study of heart and brain function, peripheral nerve and spinal cord diagnostics, as well as the localization of cancerous tissue using processed MNPs as markers (see, for example, [1–3]).

Measurements of magnetic fields that are produced purely by living biological objects and originate from tiny ionic currents in the heart tissue or in neurons in the brain using magnetocardiography (MCG) and magnetoencephalography (MEG) provide valuable information about function, pathophysiology, and health conditions. Such measurements are, however, challenging. In order to have value in medical diagnostics and research, an MCG measurement should have

a signal-to-noise ratio (SNR) that is comparable with that of electrocardiography of $\sim$100, which corresponds to a noise equivalent magnetic induction (NEMI) in the case of MCG that is lower than 10 fT Hz$^{-1/2}$ in the 1 Hz–1 kHz frequency range. A similar sensitivity and frequency bandwidth are required for sensors that are used in MEG to detect and characterize deep sources of magnetic field in the human brain. Sufficient sensitivity and frequency bandwidth for biomagnetic measurements in the presence of relatively large background magnetic fields of >100 nT can currently only be achieved by using special sensors ('biomagnetometers') that are based on superconducting quantum interference devices (SQUIDs).

Another promising technique for neuromagnetic recording utilizes atomic magnetometers (also referred to as optically-pumped or spin exchange relaxation-free magnetometers). It has been shown [4] that an optical-spectroscopy-based chip-scale atomic magnetometer sensor with a magnetic sensitivity of $\sim$200 fT Hz$^{-1/2}$ at 10 Hz is able to record spontaneous and somatosensory evoked neuromagnetic fields. Johnson *et al* used this technology to measure brain response from auditory and median nerve stimulation [5]. Although atomic magnetometers are promising because they do not require cooling, a problem with the current technology is that the sensitivity ($\sim$15 fT Hz$^{-1/2}$), dynamic range, and a too narrow frequency bandwidth ($\sim$10 Hz) of the sensors are not sufficient for processing most MEG signals. Improvements have recently been reported, where the authors claim that new atomic magnetometers provide a NEMI of better than 1 fT Hz$^{-1/2}$ and do not need to be shielded from the Earth's magnetic field [6]. Theoretical studies [7, 8] have shown that atomic magnetometers can provide a higher SNR and potentially replace SQUIDs in MEG systems. A recent publication [9] also shows a capability of neuromagnetic source localization using a single atomic magnetometer (with a NEMI of 15.9 fT Hz$^{-1/2}$ in the 2–80 Hz frequency range) placed sequentially at 13 locations. However, an increase in the frequency range is an issue because the sensitivity and frequency bandwidth of such a sensor technology are mutually incompatible [10]. The issue of cross-talk between sensors that are in close proximity to one another will also be significant, due to either diffusion of the gas from one laser readout beam to another or mutual inductance between feedback coils surrounding the gas enclosures. Furthermore, the utilization of atomic magnetometers for neuromagnetic recording in less shielded environments is limited by the dynamic range of the readout electronics. In contrast, SQUIDs can be configured as gradiometric superconducting flux transformers that intrinsically remove environmental noise during measurements by recording the gradient of the magnetic flux. Moreover, flux counting readout electronics with a dynamic range of $\sim$130 dB and a slew rate of about 5 MΦ_0 s^{-1} can be used with low- and high-T_c direct current (DC) SQUIDs [11].

Nearly all biomagnetometers in commercially available MCG and MEG measurement systems rely on low-T_c SQUIDs that operate at temperatures below 9 K and are typically cooled with liquid helium. The use of liquid helium as a coolant is inconvenient for medical personnel and results in enormous operating costs, thereby preventing the widespread distribution of such systems in ordinary hospitals. The prospect of changing to liquid-nitrogen-cooled high-T_c SQUIDs in future biomagnetometer systems would eliminate the dependence on increasingly unreliable helium supplies [12] and reduce risk for end users, while relaxing the demands that are placed on them. It would also save a large fraction of the operating costs. It is expected that the total cost (investment plus operating cost) of each high-T_c biomagnetometer system would only be about half that of a corresponding low-T_c system. When compared to a liquid helium system, the liquid nitrogen cryostat design is far simpler, reducing the overall system cost. The cryogen itself also has a much lower evaporation rate and is plentiful, meaning that running costs are far lower. As such, high-T_c SQUID technology may stimulate the acceptance of biomagnetometer systems for more widespread clinical use. High-T_c biomagnetometer systems have the added advantage that cryostats with smaller separations between the superconducting sensor and the room temperature environment of biologically active objects are possible. The improved sensor-to-source proximity leads to higher SNR and better representation and characterization of the true source signal. For example, the dipole nature of magnetic field sources in biological objects provides a boost in signal power to high-T_c sensors that are within 1 mm of a room temperature object. The SNR (e.g., in MEG recordings) can then be high enough that a relatively large biomagnetometer sensor NEMI of about 50 fT Hz$^{-1/2}$ at 77 K can be acceptable [13–15]. However, state-of-the-art noise levels in high-T_c technology (<10 fT Hz$^{-1/2}$ in the 1 Hz–1 kHz frequency range) are paramount for making biomagnetometer systems that are not only cheaper and more accessible than their predecessors, but also significantly better in terms of providing relevant clinical diagnostic and monitoring information and surgical guidance.

When compared to their low-T_c predecessors, high-T_c biomagnetometers currently have limited clinical utility because their technology is still too sophisticated and has yet to reach the level of maturity that is needed for mass production. The reasons for this situation are multifold. In contrast to low-T_c Nb technology, the most successful material technology for high-T_c SQUIDs to date is YBa$_2$Cu$_3$O$_{7-x}$ (YBCO), a ceramic oxide superconductor that has intrinsic complications, including a much shorter coherence length, d-wave symmetry of the superconducting order parameter, and relatively weak pinning forces at liquid nitrogen temperature. All of these issues demand very different technologies for the preparation of films, Josephson junctions (JJs), and thin film multilayer heterostructures, when compared to low-T_c technology. High-T_c YBCO SQUIDs must be made from high quality thin film epitaxial heterostructures in an oxygen atmosphere at a relatively high substrate temperature of $\sim$800 °C. Currently, the best high-T_c sensor technology consists of DC SQUIDs that are coupled to thin film superconducting multilayer flux transformers. Their fabrication is so challenging that only a handful of dedicated research groups have managed to produce high-T_c SQUIDs that have white noise levels of below 10 fT Hz$^{-1/2}$ (at 77 K) at

frequencies of above a few Hz [16–20]. The main challenge is to avoid excessive $1/f$ low frequency noise in the high-T_c superconducting thin film multilayer flux transformer, which can originate from the presence of parasitic grain boundaries (GBs) in the top epitaxial YBCO film, especially near the edges of the underlying layers, and/or due to degraded superconducting parameters in the bottom YBCO film.

In this paper, we provide an overview of the sensor technology, measurement system construction, and examples of applications of currently available high-T_c biomagnetometers. We outline the deposition and structuring of the epitaxial oxide heterostructures, materials for substrates, epitaxial bilayer buffers and multilayer flux transformers, and step-edge and bicrystal JJs. We also present the layout and properties of epitaxial multilayer high-T_c DC SQUID sensors, as well as their integration in measurement systems with special electronics and liquid nitrogen cryostats for different applications. Future challenges in the field are then addressed.

2. Experimental technique

In this section, the technology and related properties of high-T_c DC SQUID biomagnetometer sensors, their integration in high-T_c biomagnetic measurement systems with liquid nitrogen cryostats and SQUID readout electronics are described. High-T_c DC SQUID sensors were separately produced at Forschungszentrum Jülich GmbH (Jülich) and at Chalmers University of Technology (Chalmers) using different technologies. The Jülich technology includes high-oxygen-pressure sputtering [21] for the deposition of YBCO films, step-edge JJs [22] for high-T_c DC SQUIDs and superconducting multilayer thin-film flux transformers with the input coil inductively coupled to the SQUID loop in a flip-chip configuration. At Chalmers, laser ablation for the deposition of YBCO films, bicrystal JJs [23] for DC SQUIDs and direct-coupled high-T_c DC SQUIDs (with the pickup loop made on the same substrate as the SQUID and galvanically connected to the SQUID loop) were used. Jülich used modulation DC SQUID electronics and cryostats, which were developed at the Kotel'nikov Institute of Radio Engineering and Electronics RAS and produced at Cryoton Co. Ltd [24], while Chalmers used direct amplification electronics from Magnicon and cryostats from ILK Dresden [25].

2.1. High-T_c DC SQUID biomagnetometer sensors

Bicrystal JJs are one of the earliest technological developments in high-T_c DC SQUID fabrication [23]. The process is advantageous because it is simple and reproducible, although it suffers from a lack of readily-available high quality bicrystal substrates, as well as limited design freedom imposed by the fact that the placement of JJs is constrained to the bicrystal boundary.

The Chalmers bicrystal high-T_c DC SQUID biomagnetometer sensors are made on 1 mm thick bicrystal SrTiO₃ (STO) substrates with a 24° misorientation angle. An ultra-high-vacuum pulsed laser deposition system (DCA

instruments) is used to deposit 200–300 nm thick YBCO films on the bicrystal substrates. A seed layer of between 20 and 50 nm of CeO₂ may be included for improving the epitaxy of the YBCO. During YBCO deposition, the oxygen pressure is maintained at 0.5–1.0 mbar. The sample is annealed over ∼2 h at a temperature of 500 °C–600 °C, in order to ensure proper oxygen doping. Ar ion beam etching (IBE) and standard photolithography are used to pattern single layer bicrystal high-T_c DC SQUID biomagnetometers. Further details about film deposition, design, and fabrication can be found elsewhere [26, 27].

Each of the Jülich step-edge high-T_c DC SQUID biomagnetometer sensors was made on two separate 1 mm thick single crystal (001) oriented MgO substrates: one 10 mm × 10 mm substrate for two SQUIDs and one 30 mm diameter wafer for a superconducting flux transformer. The low cost and good availability of single crystal MgO substrates, a thermal expansion coefficient of ∼13.4 × 10^{-6} K^{-1} that matches well with YBCO, a low dielectric constant ($\varepsilon \sim 10$) and low microwave losses ($\delta \sim 10^{-6}$) are all decisive advantages of using MgO as a substrate material for the preparation of heterostructures with YBCO. The lattice mismatch between YBCO and MgO is ∼9% for a cube-on-cube mutual orientation. Although this mismatch results in difficulties for the cube-on-cube epitaxial growth of YBCO films on MgO, it facilitates growth on other crystallographic planes and graphoepitaxial growth. We take advantage of the fact that an YBCO film grows c-axis-oriented on 45° tilted MgO substrates [28], as well as on the surfaces of 45° tilted step edges on (001) MgO substrates [20]. At interfaces/step-edges between these crystallographic orientations on the substrate, c-axis-oriented layers of YBCO consistently form two symmetrical GBs with an exact 45° [100]-tilted misorientation angle between them. Surprisingly, this situation can be achieved despite slight deviations in the slope angle of the step edges from an exact 45° value [20]. High quality and relatively smooth (droplet-free) YBCO films are deposited by high oxygen pressure sputtering in pure oxygen (99.999%) at a pressure of ∼3 mbar [21].

Ar IBE and the negative photoresist nLOF2020 were used for the preparation of 45° steps on (001) MgO substrates (see the scanning electron microscopy (SEM) images in [29]). A second ion beam milling step was used to clean the surface [20, 30], in order to remove residual resputtered material, including undesirable 'fences' that appear when resputtered material gathers at the top corners of the steps during the first ion beam milling procedure. A much longer ion beam milling step was additionally used to texture the surface of the MgO substrate in the form of linear trenches along the [100] and [010] directions [20, 22, 29]. The bottom corner of the step was smoothed due to the simultaneous effect of the angular dependence of ion beam milling and the partial redeposition of etched material.

The 45° slope of the step edges on MgO is gentle enough for the homogeneous deposition of thin film buffer layers by high oxygen pressure sputtering. The homogeneity and quality of the superconducting YBCO films was improved significantly by the introduction of a double buffer
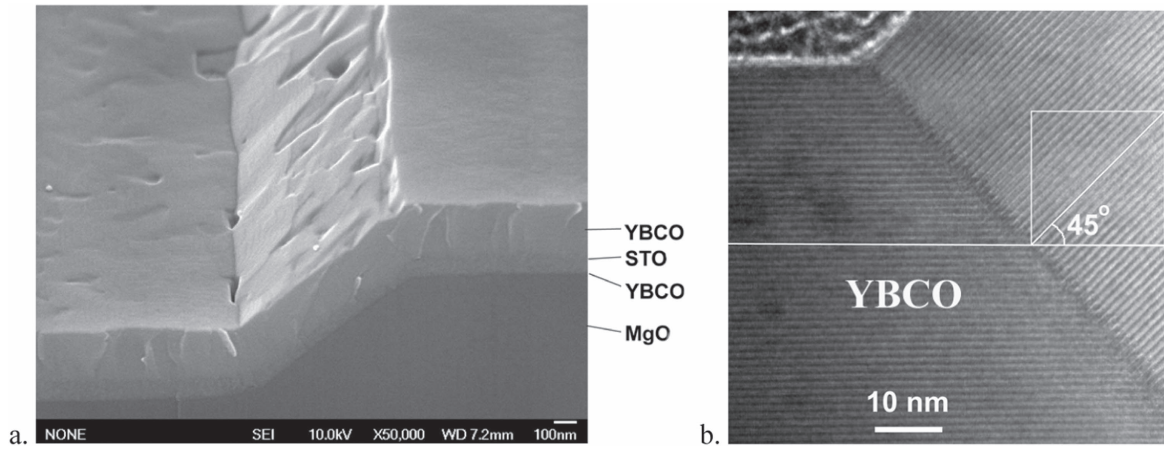
Figure 1. (a) SEM image of an YBCO film deposited on a double-layer-buffered 45° step on an MgO substrate. The image was obtained with the sample cut perpendicular to the step. (b) HRTEM image of a 45° [100]-tilted GB in the top YBCO layer at the lower corner of the step.

layer: a bottom 10 nm thick non-superconducting YBCO film as a 'seed' layer that was covered by a 30 nm thick SrTiO$_3$ (STO) film as a 'blocking' layer [29]. Figure 1 shows an SEM image of an YBCO film deposited on such a double-layer-buffered 45° step on an MgO substrate, as well as a high-resolution transmission electron microscopy (HRTEM) image of the 45° [100]-tilted GB in the top (super-conducting) YBCO layer at the lower corner of the step. The top YBCO layer had a thickness of ~200 nm, a T_c of ~93 K and a critical current density of ~5 MA cm^{-2} at 77 K. We protected the superconducting film with a 5 nm thick Pt film that passivated the junctions and provided a better electrical contact for bonding.

The surface texturing changes the in-plane orientation of the YBCO film on the MgO substrate and step edges. SEM images of the surface of the YBCO film in the step-edge area show rectangular growth spirals with 1 nm high steps between flat areas [31]. The orientations of such spirals indicate that all of the grains in the YBCO film are aligned in-plane, with their a- or b-axes normal to the corners of the step. In this case, the superconducting critical current density is maximized and constant along both GBs. Such texturing of the MgO surface also helps to increase the relevant JJ parameters, reduce the meandering of GBs, and improve the overall characteristics of the SQUIDs.

High-T_c JJs are made by patterning bridges of width $w \sim 2\,\mu$m in the YBCO-STO-YBCO heterostructure across the substrate step. Both the upper and the lower GBs in each step-edge junction have similar cross-sections and mis-orientation angles and, consequently, similar critical currents and normal state resistances R_n. They are connected serially and act together synchronously as a single JJ with twice the normal state resistance and half of the capacitance of a single GB. For such an effective JJ, a total capacitance C of ~10 fF, a normal state resistance R_n of ~20 Ω, and a characteristic voltage $V_c = I_cR_n$ of ~800 μV at 77 K were obtained from the analysis of the $I(V)$ characteristics of the junction. A capacitance C of ~10 fF of step edge JJs on an MgO substrate was reported previously [32]. Such a low capacitance of a high-T_c

JJ is advantageous for lowering the intrinsic flux noise S_Φ of high-T_c DC SQUIDs made with such JJs [33, 34]:

$$S_\Phi \approx 32k_BTL_S(L_SC/\beta_C)^{1/2}, \qquad (1)$$

where L_S is the SQUID loop inductance, $\beta_C = 2\pi I_C R_n^2 C /\Phi_0 \approx 0.4$ is the Stewart–McCumber parameter of the JJ and the magnetic flux quantum $\Phi_0 = h/2e = 2.068 \times 10^{-15}$ T m^2, where h is the Planck constant and e is the electron charge. The Stewart–McCumber parameter remains almost constant for high-T_c JJs of different width and/or cross-sectional area, whereas in the case of low-T_c JJs the normal state resistance R_n is determined by the shunt resistor and is independent of the JJ area.

Comparing the intrinsic flux noise of low-T_c and high-T_c SQUIDs is illustrative of other benefits that are inherent to high-T_c technology. For example, the far lower operating temperatures of low-T_c SQUIDs should reduce their intrinsic noise levels S_Φ when compared to high-T_c technology by a factor of $77/4.2 \sim 20$. This factor is, however, almost compensated by the ~100 × higher capacitance of Nb-based planar JJs (~1 pF), resulting in comparable NEMI values of ~5 fT Hz$^{-1/2}$ for high-T_c and low-T_c SQUIDs, in spite of the much higher operating temperature of high-T_c SQUIDs.

For applications of DC SQUIDs, the spread in JJ critical current should be as low as possible, and preferably below 10%. This spread depends on the morphologies of the GBs and on the precision of the patterning of the YBCO films. 45° [100]-tilted GBs on step-edge JJs on MgO are very straight: their deviation is ≪100 nm, which is significantly smaller than the ~200 nm deviation of the 24° [001]-tilted GBs in bicrystal-substrate-based JJs [19]. More than 100 step-edge JJs with 45° step edges on MgO substrates were prepared during optimization of the technology. The observed spreads in critical current $\delta I_c/I_c$ and I_cR_n product depend on the microstructural quality of the JJs. Without using an STO blocking layer, typical values for $\delta I_c/I_c$ of ~20% and for the I_cR_n product of ~300 μV were measured at 77 K [20]. Meandering of the GBs and mutual misorientation of grains in the YBCO film at the step edge area were reduced by properly texturing the MgO substrates after step preparation. The STO

blocking layer has a reduced density of holes and precipitates in the YBCO film. As a result, the spread in critical current $\delta I_c/I_c$ was reduced to $\sim$10% [29] and values of the I_cR_n product of up to $\sim$800 μV were observed at 77 K. As a comparison, for bicrystal-substrate-based JJs values of the I_cR_n product of up to $\sim$400 μV at 77 K and $\sim$1 mV at 63 K were achieved [19]. At present, the spread in critical current $\delta I_c/I_c$ in 2 μm wide JJs is determined primarily by the precision of the patterning of the YBCO films of $\sim$0.2 μm using deep-UV photolithography. This value can be improved in the future by using electron beam lithography. Indeed, the most reproducible patterning of YBCO films with variations in width δw of $<$0.2 μm is achieved using electron beam lithography, a hard carbon film mask, and IBE (see for example [35] and references therein).

The operational principle of a SQUID is based on its sensitivity to changes in magnetic flux passing through its loop. The larger the SQUID loop, the more flux penetrates it for a fixed magnetic field magnitude, and thus the higher its sensitivity. However, this relationship is limited by equation (1): a larger SQUID loop leads to higher inductance and therefore lower sensitivity. Furthermore, for design reasons, a screening parameter $\beta_L = 2I_cL_S/\Phi_0 \sim 1$ should be chosen, which is a compromise between a sufficient modulation depth and a large enough value of L_S to couple flux. For a high-T_c SQUID operating at 77 K, the critical current (i.e., the Josephson coupling energy) needs to be higher than 16 μA to avoid thermal smearing and this puts a limit on the SQUID inductance $L_S \sim$ 60–100 pH. A tradeoff is therefore made, whereby the SQUID loop is kept small ($\sim$10^{-5} cm^2) and a superconducting flux transformer is used to collect magnetic flux from a relatively large area pickup loop (e.g., about 3 cm^2) and to transfer it inductively to the SQUID loop via a multiturn input coil or by direct injection of the induced current into the SQUID loop using a galvanic connection between the pickup loop and the SQUID loop.

Two types of flux transformer are referred to as 'direct-coupled' and 'flip-chip'. Direct-coupled sensors are simple to fabricate because the flux transformer can be defined together with the SQUID in a single lithography step, as is the case for single-layer sensors. Fabrication challenges associated with multilayer technology in YBCO mean that the flux transformer is typically fabricated on a second substrate that is glued to the SQUID substrate in a 'flip-chip' configuration. Despite this complication, flip-chip magnetometers are advantageous because they have much better sensitivity when compared to direct-coupled magnetometers. The effective area A_{eff} is $\sim$10$\times$ larger for flip-chip designs, when compared to equivalent direct-coupled designs in the case of 20 mm pickup coils. This gain increases as a function of the size of the pickup coil because direct-coupled sensors suffer from an increasing inductance mismatch between the large pickup coil and the SQUID. This mismatch can be mitigated in the more flexible flip-chip design by careful selection of flux transformers with inductances of the pickup coil and input coil that are approximately equal to each other. The effective area of such a flip-chip magnetometer $A_{eff} \sim A_{pu}/\sqrt{L_{pu}} \sim a^{3/2}$, where A_{pu} is the area, L_{pu} is the inductance, and 'a' is an approximate measure of the size (i.e., the diameter of a circular loop or the side dimension of a square loop) of the pick-up loop of the flux transformer. The flip-chip approach is currently the only method that has achieved the required values of NEMI of below 10 fT Hz$^{-1/2}$ at 10 Hz and 77 K.

Our high performance high-T_c superconducting multi-layer flux transformer is made from epitaxial thin-film heterostructures that contain two high-T_c superconducting layers of YBCO separated by an insulating layer, which consists of $PrBa_2Cu_3O_{7-x}$ (PBCO) and STO thin films [36]. A critical process that is needed for the preparation of high-T_c superconducting multilayer thin film flux transformers is based on chemical wet etching in Br-ethanol solution [37]. This step is used to pattern the bottom YBCO film, while preventing issues that are critical for multilayer epitaxy and unavoidable when IBE is used: the creation of 'fences' at the edges of the photoresist mask and ion-beam-induced damage to the substrate surface. Appropriate superconducting parameters of all of the superconducting films are a prerequisite for the preparation of low-noise biomagnetometers, especially in the low frequency range. GBs should be avoided in the top YBCO layer because they cause increased $1/f$ noise of the sensor [38]. Chemical etching results in gently sloping edges of the patterned structures, which are advantageous for avoiding GBs in the top YBCO layer [37]. The input coil includes a $\sim$200 nm bottom YBCO film that is covered by a $\sim$400 nm thick layer of PBCO-STO insulator and a 600–1000 nm top YBCO film. The dynamic range of the flux transformer is limited by the critical current of the input coil, which is proportional to the thickness of the top YBCO film. It should be noted that oxygenation of the bottom YBCO layer should be performed despite the presence of the STO insulator layer deposited above it. Fortunately, STO enables sufficient diffusion of oxygen ions for oxygenation of the bottom YBCO film at a substrate temperature of $\sim$500 $^\circ$C. The empirically-obtained time required for the full oxygenation of a bottom YBCO film covered by a 0.5 μm thick STO film is $\sim$2 h at 500 $^\circ$C. The gently sloping edges of patterned structures and full oxygenation of the YBCO films have helped to avoid increased $1/f$ noise of the superconducting multilayer flux transformers.

A schematic diagram of the SQUID flip-chip magnetometer with coupling to control electronics and a schematic 3D layout demonstrating the flip-chip arrangement of the SQUID, flux transformer and modulation coil are shown in figures 2(a) and (b), respectively. The SQUID has a 1 mm washer and a 3 mm direct-coupled pick-up loop. The 14-turn input coil of the flux transformer is inductively coupled to the SQUID washer, while the direct-coupled loop is inductively coupled to the modulation/feedback coil of the SQUID readout electronics and also serves as one of the superconducting electrodes for current biasing of the SQUID.

High-T_c superconducting flux transformers with multi-turn input coils can be made on STO, LaAlO$_3$ (LAO), or MgO substrates. As for SQUID fabrication, MgO wafers have the advantage of a well-matched thermal expansion coefficient to YBCO. Sufficiently thick YBCO films, such as those typically used for the second superconducting layers of flux
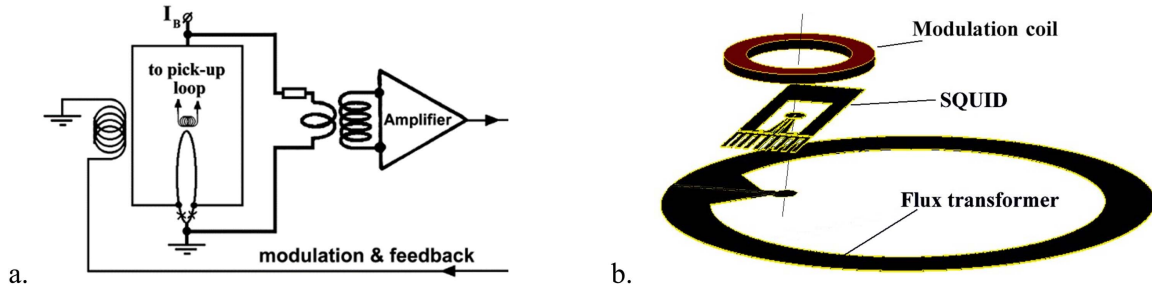
Figure 2. (a) Schematic diagram of the SQUID flip-chip magnetometer with coupling to control electronics. © 2013 IEEE. Reprinted, with permission, from [20]. (b) Schematic 3D layout demonstrating how a high-T_c superconducting flux transformer, SQUID and modulation coil are assembled together. © 2015 IEEE. Reprinted, with permission, from [39].
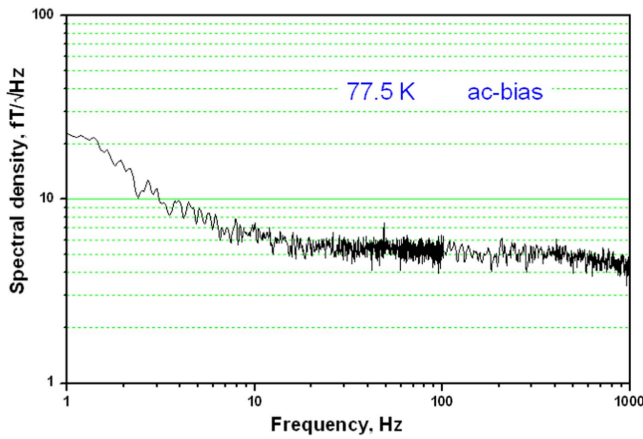

Figure 3. Noise spectral density of a 16 mm high-T_c DC SQUID magnetometer with step-edge junctions measured in a super-conducting shield. © 2013 IEEE. Reprinted, with permission, from [20].

transformers, develop cracks when they are deposited on STO and LAO substrates, whereas no cracks are observed for YBCO films that are as thick as 5 μm and are grown on MgO substrates [40]. A noteworthy limitation for the use of MgO substrates is that they require epitaxial double-layer buffering.

The preferred seed layer for the preparation of flux transformers is BaZrO$_3$ (BZO) because its lattice constant is similar to that of MgO, its crystal structure is similar to that of the second (STO) buffer layer that is destined to grow on top of it, and it is insensitive to the Br-ethanol solution that is used for patterning the bottom YBCO layer. This epitaxial BZO–STO buffer layer also protects the hygroscopic surface of the MgO substrate against degradation in air and during lithographic procedures. Whereas antiphase boundaries at the BZO–MgO interface have been observed to spread through the BZO layer, they usually disappear at the STO–BZO interface [41]. The STO layer initially grows with an expanded lattice constant to match that of the underlying BZO. However, within a few unit cells of the STO–BZO interface the STO lattice constant relaxes to its bulk value. The surface of the STO layer on which the top YBCO layer grows therefore has a lattice constant and a microstructural quality that are similar to those of a single-crystal STO

substrate. However, the overall thermal expansion coefficient is still determined by the 1 mm thick MgO wafer.

Figure 3 shows an example of the noise spectral density of a 16 mm high-T_c DC SQUID flip-chip magnetometer with step-edge junctions measured inside shields consisting of three layers of μ-metal and one of a high-T_c superconductor. The effective area A_{eff} and the flux-to-field transformation coefficient of this magnetometer are approximately 4.6 mm^2 and 0.45 nT/Φ_0, respectively. In the white noise region above $\sim$10 Hz, the magnetic flux noise $\sqrt{S_\Phi}$ and NEMI are approximately 10 $\mu\Phi_0$ Hz$^{-1/2}$ and 5 fT Hz$^{-1/2}$, respectively, at 77 K. The NEMI B_N can be estimated based on the properties of the SQUID, the flux transformer, and the coupling between the two, according to the equation

$$B_N = \frac{L_{pu} + L_i}{k A_{pu} \sqrt{L_i L_S}} S_\Phi^{1/2}, \qquad (2)$$

where $L_S \cong 100$ pH and $L_i \cong L_{pu} \cong 40$ nH are the inductances of the SQUID loop and the input coil, respectively, while $k \cong 0.7$ is the coupling coefficient and $A_{pu} \cong 256$ mm^2 is the area of the pickup loop. Below $\sim$10 Hz, additional noise in experimental recordings may be generated by the bio-magnetometer itself and external sources, e.g. Abrikosov vortex creep in the superconducting shield or residual laboratory environmental noise coupling via electrical connections. Increased low frequency noise of the SQUID can also be a first indication of ageing in one of the super-conducting films of the SQUID and/or superconducting multilayer flux transformer.

Ageing is a significant problem for YBCO films, as their performance is highly dependent upon their oxygen doping and chemistry, both of which are extremely sensitive to the environment. The degradation of the superconducting parameters of YBCO films can be prevented by ensuring vacuum-tight encapsulation of the magnetometers. An example of such a capsule is shown in figure 4. Encapsulated sensors have lower intrinsic noise and longer-term stability because the vacuum-tight capsule dampens external thermal fluctuations, isolates them from ambient air and humidity, and provides mechanical protection of the sensors, thereby ensuring a long and reliable service life. This is especially important for delicate flip-chip sensors with multilayer flux transformers. Encapsulation also significantly simplifies their
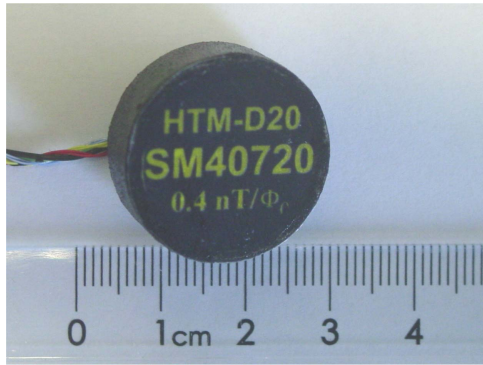
Figure 4. Photograph of an encapsulated high-T_c biomagnetometer that includes a superconducting flux transformer with a round pick-up loop, whose outer diameter is 20 mm. The button-shaped fiberglass capsule has an outer diameter of $\sim$24 mm and a total thickness of $\sim$10 mm.

handling during characterization, applications, and for end users.

The best results were obtained by using vacuum-tight encapsulation of the sensors in fiberglass-reinforced epoxy capsules. Such packaging includes the SQUID with the multilayer flux transformer, as well as a heater, RF filters, and a feedback coil. A thin film Pt PT-100 resistor can be used as a thermometer and a heater. The use of the heater allows easy removal of trapped magnetic flux to improve the low frequency noise properties of the sensor during day-to-day use. If necessary, the fiberglass capsule can be opened for adjustment or repair of the sensor. Figure 4 shows a photograph of an encapsulated high-T_c DC SQUID biomagnetometer. The encapsulation does not add significantly to the lateral size of the sensor. The superconducting flux transformer of the encapsulated sensor in figure 4 has a round pick-up loop with an outer diameter of 20 mm. The outer diameter of the vacuum-tight enclosure is $\sim$24 mm (the total thickness is $\sim$10 mm). Dense packing of multiple sensors, e.g., for MEG, is therefore possible. The effective area A_{eff} and the field-to-flux transformation coefficient of this magnetometer are approximately 5.17 mm^2 and 0.4 nT/Φ_0, respectively. The characteristics of the magnetometers have not changed after more than ten years of storage and multiple tests that include thermal cycling.

Chalmers has produced 'directly-coupled' high-T_c biomagnetometers on 10 mm bicrystal STO substrates that have an in-plane misorientation angle of 24° [13]. The preparation of such sensors includes only a single layer of YBCO and is much simpler when compared to the multilayer technology described above. However, the typical NEMI (of about 50 fT Hz$^{-1/2}$ at 10 Hz and 77 K) is much higher than the NEMI of flip-chip magnetometers. The higher NEMI values impose restrictions on the construction and possible applications of biomagnetic measurement systems. In order to achieve comparable SNR values for the same measurement time, the sensor should be placed much closer to the object in the case of MEG measurements. However, for the recording of MCG and magnetic signals originating from MNPs, a NEMI value of 50 fT Hz$^{-1/2}$ at 10 Hz and 77 K appears to be sufficient.

2.2. Cooling of high-T_c DC SQUID biomagnetometers

High-T_c biomagnetometers operate at $T \sim$77 K, which corresponds to an optimal value of the Stewart–McCumber parameter $\beta_c \sim 0.4$ of the bicrystal and step-edge JJs. The cheapest and most convenient cooling method is to simply immerse the sensors in liquid nitrogen at normal atmospheric pressure. The price of liquid nitrogen is presently $\sim$300 times lower than that of liquid helium ($\sim$15 €l^{-1} for liquid helium and $\sim$0.06 €l^{-1} for liquid nitrogen). This difference in price is expected to grow, as helium is a finite resource, whereas nitrogen comprises $\sim$80% of the atmosphere. Liquid nitrogen is also $\sim$60 times more efficient in terms of cooling power. The heats of vaporization of helium and nitrogen are 2.68 J l^{-1} and 161 J l^{-1}, respectively. High-T_c biomagnetometers can therefore be cooled in cryostats that have fewer radiation shields and can be placed closer to the outer wall/room temperature environment than low-T_c biomagnetometers. In a standard low-T_c MEG system, the spacing between the pickup loop of the sensors and the room temperature cryostat surface is typically $\sim$20 mm. For a high-T_c system with a similar cryogen consumption (boil-off rate), this spacing can be below $\sim$5 mm. From a practical perspective, the hold time of a liquid nitrogen cryostat is on average about five times longer than that of a liquid helium cryostat. This difference promises to increase the availability of high-T_c biomagnetometer systems when compared to low-T_c technology, while reducing the person-hours needed to maintain them. For example, a 50 l liquid-nitrogen-based full-head MEG system can run continuously for more than a month without being refilled. In contrast, the time period is $\sim$1 week for a 100 l liquid-helium-based MEG system that is presently state-of-the-art.

The relaxed cooling requirements of high-T_c biomagnetometer technology result in an additional benefit of a reduced spacing between the sensor and the object, i.e., the biomagnetic source. A smaller distance between the biomagnetometer and the object leads to improved signal levels arising from dipolar-like sources that generate the biomagnetic fields. The magnitude of the magnetic field generated by current dipoles, such as those associated with neuromagnetic activity recorded in MEG, decays as $\sim 1/r^2$ with distance r between the biomagnetometer and the object. For magnetic dipoles, such as those associated with MNPs, the equivalent dependence is $\sim 1/r^3$. As such, a reduction in spacing, r, by a factor of 3 (which is reasonable when comparing cryostats for high-T_c and low-T_c SQUIDs) leads to an order of magnitude gain in signal magnitude. For similar NEMI values and sensor sizes, the SNR obtained during the detection of superficial sources of biomagnetic signals by a high-T_c biomagnetometer system can therefore be significantly higher than that for a low-T_c biomagnetometer system. The spatial resolution can also be enhanced because biomagnetic fields can have higher spatial frequencies at an object surface. For example, in the case of MEG, 40% more information can be obtained from the human brain by using a high-T_c MEG system when compared to the state-of-the-art in a low-T_c MEG system [14]. If enhanced signal amplitude of the high-T_c biomagnetometer system does not benefit a particular
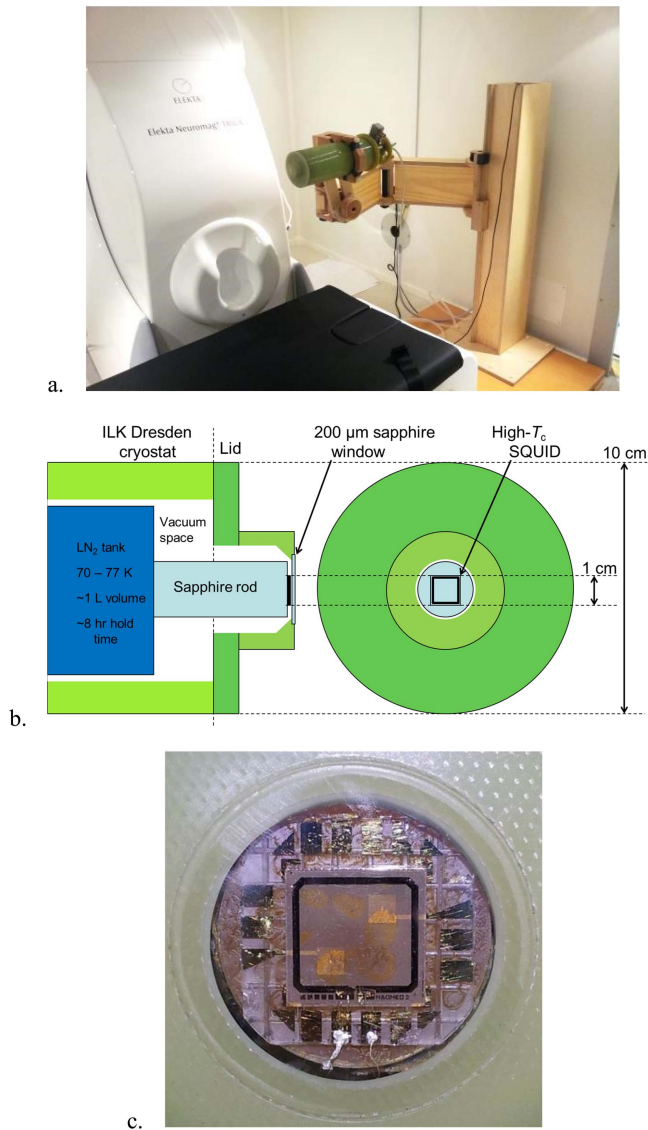
Figure 5. (a) Photograph of the Elekta Neuromag TRIUX system and biomagnetometer in the ILK Dresden cryostat at the Karolinska Institute's NatMEG laboratory. © 1969 IEEE. Adapted, with permission, from [15]. (b) Cutaway schematic diagram of the cryostat. (c) Photograph of the 'direct-coupled' high-T_c DC SQUID magnetometer used for MEG recordings, as it sits on top of the sapphire rod that is thermally anchored to the liquid nitrogen bath behind the thin room temperature sapphire window of the cryostat.

application, then it can be balanced by a reduction in the total system cost by using less sensitive SQUIDs and/or reducing the magnetic shielding.

The first tests of the Chalmers 'directly-coupled' high-T_c biomagnetometers for magnetic immunoassays (MIAs) and MEG were performed using a fiberglass-reinforced epoxy cryostat with a 1 l liquid nitrogen tank and a hold time at the base temperature $T \sim 73$ K of approximately 8 h, as shown in figure 5. The cryostat was developed and produced by ILK Dresden [25]. We pump on the liquid nitrogen bath to reduce its boiling temperature and to achieve an operating temperature below 77 K. A thermal link connects the liquid nitrogen bath to a sapphire rod, on which the SQUID chip is mounted, such that the cryostat can be operated both in the standard

'sensor down' and at arbitrary, including 'sensor up', tilt angles. Furthermore, the sensor is housed in vacuum behind a thin (200 μm) sapphire window at room temperature. In order to reduce the thermal load of ambient radiation, the window can have a thin layer of reflective Au deposited on its backside. However, the Au should be patterned in the form of a 5 mm grid to limit the conducting paths of eddy currents that could otherwise contribute to increased values of NEMI. Micrometer screws support the inner liquid nitrogen + sensor structure so that it can be raised and lowered with respect to the room temperature window. Careful adjustment of the screws while the cryostat is cold allows the high-T_c biomagnetometer to be placed within less than 1 mm of the room temperature environment, while maintaining its operating temperature.

First tests of Jülich 'flip-chip' high-T_c biomagnetometers for MCG and MEG were performed using a fiberglass cryostat with a 1.5 l liquid nitrogen tank and a hold time of 10 d. The cryostat was developed and produced by Cryoton Co. Ltd [24]. The cold–warm distance at the cryostat bottom is about 10 mm. Two encapsulated 16 mm high-T_c biomagnetometers with NEMI values of $\sim$5 fT Hz$^{-1/2}$ at 77 K were fixed 'on-axis' parallel to each other on a fiberglass holder and immersed in liquid nitrogen, as shown in figure 6. The electronic gradiometer baseline of 10 cm is determined by the distance between the flux transformers of the magnetometers. The bottom sensor is intended for detection of the signal from the object, while the top magnetometer serves as a reference, e.g., for reducing environmental noise. The distance between the pickup loop of the bottom magnetometer and the outer surface of the cryostat is about 15 mm. Both the ILK Dresden and the Cryoton single (signal) channel cryostats are convenient for sensor development proof-of-principle tests for different applications. However, they should be replaced by a multi-channel system, e.g., for practical use in MCG or MEG.

The use of a multichannel biomagnetometer system for MCG and MEG saves measurement time and also allows better localization and characterization of sources of magnetic field in the heart and brain, respectively. The sensors should be placed in a dense array and located as close as possible to the chest/scalp and to neighboring sensors. Cross-talk measurements [39] have confirmed the possibility of building such closely-packed arrays of high-T_c biomagnetometers. Encapsulated high-T_c biomagnetometers are sufficiently small that more than 100 sensors can be placed above and around an adult human head in the form of a single helmet-shaped cryostat. One limitation to such an approach is that the variety of individuals' head sizes and shapes requires varying the spacing between the sensors and the scalp and thus reduced proximity to some brain regions. This problem is inherent to state-of-the-art MEG systems, but can be overcome by using high-T_c biomagnetometer systems that are designed with a mechanically flexible set of cooling systems that can be adjusted to maintain close proximity between each sensor and the scalp.

In principle, each channel can be placed in an individual cryostat that has a small area at its lower end and is adjusted individually to the scalp [42]. The advantage of such a
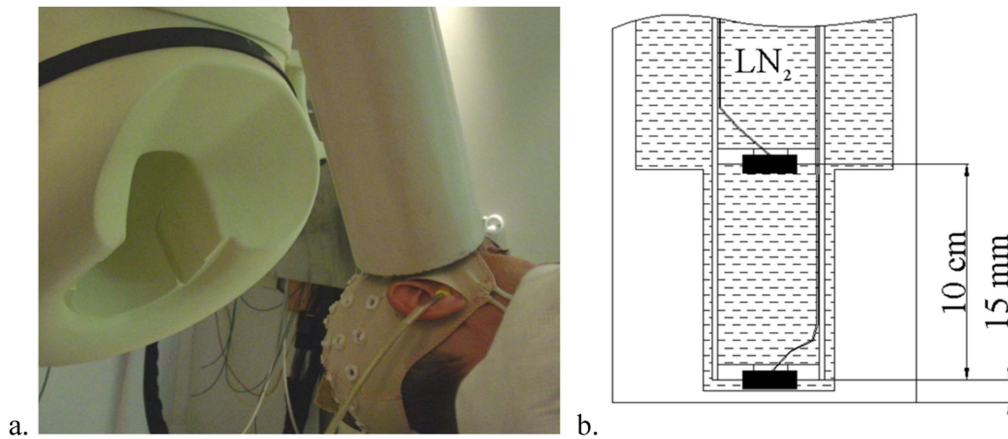
Figure 6. (a) Photograph of high-T_c and whole-head low-T_c systems taken during the measurement of an auditory evoked field. Reprinted from [42], Copyright 2012, with permission from Elsevier. (b) Schematic diagram of two high-T_c biomagnetometers immersed in liquid nitrogen in a fiberglass cryostat.

segmented helmet construction is the possibility to realize a SQUID-to-scalp separation down to <3 mm by using a very thin wall at the bottom end of a small cryostat. The main disadvantage is the increased tangential separation between the channels due to the sidewalls of the cryostat, which can lead to attenuation of high spatial frequencies in the MEG signals. However, cryogen transfer and cryostat costs are less critical for high-T_c systems when compared to low-T_c systems, as suggested in [42]. Cryogen-free cooling systems (see, e.g., [43]) can also be used, provided that their magnetic noise is sufficiently low.

High-T_c biomagnetometers may be placed very close (at a distance of <3 mm) to the scalp by fixing them in the vacuum space of a cryostat inside thermal conducting sockets and cooling them sidewards, for example with the help of vacuum grease. Alternatively, the sensors can be placed in liquid nitrogen inside individual dimples on the inner side of the cold wall.

2.3. Readout electronics for high-T_c DC SQUID biomagnetometers

At an optimal bias current, the SQUID voltage V is periodic as a function of magnetic flux Φ through the loop of a DC SQUID, with a period given by the flux quantum Φ_0. Linearization of the $V(\Phi)$ transfer function is provided by SQUID readout electronics operating in a flux-locked loop mode using a modulation scheme [44] or direct amplification [45]. The primary advantage of the modulation scheme is an increase in the readout voltage signal that is available to the field effect transistor in the first amplification stage of the SQUID readout electronics. This is caused by a boost in effective SQUID output impedance by the application of a matching transformer that serves as a low-noise preamplifier. The primary disadvantage of the modulation scheme is that the bandwidth, which is typically ∼20 kHz, is limited by the lock-in demodulation circuit. However, because most relevant biomagnetic signals do not contain useful information above a few kHz, a 20 kHz sensor bandwidth is sufficient for most biomagnetic applications.

The critical currents and normal resistances of JJs constituting DC SQUIDs have low frequency fluctuations with a spectral density $S \sim 1/f$. In the case of low-T_c DC SQUIDs with Nb–Al$_2$O$_3$–Nb tunnel JJs, these fluctuations are weak and barely affect the SQUID low frequency noise [46]. On the other hand, these fluctuations are the dominant source of $1/f$ noise in high-T_c DC SQUIDs [47]. In-phase fluctuations of the critical current are eliminated by using the 'standard' flux modulation scheme with negative feedback. Readout electronics with an additional bias-reversal modulation scheme intended for the reduction of $1/f$ noise originating from out-of-phase critical-current fluctuations were proposed a long time ago (see [47–49]) and have been included in commercial SQUID electronics units (from, e.g., Tristan Technologies, Magnicon, EZ SQUID, Supracon, STAR Cryoelectronics and Cryoton). The bias reversal circuit simultaneously switches the polarities of the bias current and the magnetic flux, thereby effectively canceling the out-of-phase critical-current fluctuations, while the system remains sensitive to changes in the $V(\Phi)$ curve due to the external magnetic flux. Bias reversal effectively reduces the 'knee frequency' (at which the $1/f$ and white noise contributions to the power spectral density are statistically equal) from a few kHz to a few Hz.

A special high-T_c bias reversal DC SQUID readout electronics system that is used in the 'flip-chip' biomagnetometer experiments described below was developed at the Kotel'nikov Institute of Radio Engineering and Electronics RAS and produced by Cryoton Co. Ltd [24, 50]. The modulation and bias-reversal signals are formed in each channel by a programmable logic device. Furthermore, the implementation of correct compensating signals and the removal of transient voltage peaks generated by parasitic inductances during switching of bias current are allowed. In this high-T_c SQUID readout electronics system, the current-bias-reversal and modulation signals are rectangular, with a frequency of the modulation signal that is twice that of the current-bias-reversal. Two special compensation signals help to remove the residuals of the current-bias-reversal in the primary winding of the matching transformer and to compensate, e.g.,

the slight asymmetry in the critical currents of the JJs in a given SQUID. In order to reduce crosstalk between the SQUID biomagnetometers, both the main and the bias-reversal modulations and feedback should be applied locally to the SQUID by a coil that has a much smaller outer size when compared to the size of the pickup loop [39]. Direct injection of current into the SQUID loop [51, 52] is another possibility for generating a locally applied modulation-feedback signal, which is convenient for single-chip integrated DC SQUID magnetometers.

3. Applicability test for high-T_c DC SQUID biomagnetometers

In this section, a primary focus is placed on experiments that demonstrate the applicability of high-T_c DC SQUID biomagnetometers for MCG, MEG, and MIA measurements performed in [13, 15, 20, 53–55].

For 'direct-coupled' biomagnetometers, all recordings were carried out using ILK Dresden cryostats and Magnicon DC SQUID electronics SEL-1 with AC bias reversal. The magnetometers that were used for MEG recordings had 8 mm pickup loops. Recordings were performed in 2-layer magnetically shielded rooms (MSRs), one of which is located at Imego AB (now part of RISE Acreo) in Gothenburg and the other at the Karolinska Institute's NatMEG lab in Stockholm. In the case of MIA, a planar gradiometer was used with a figure-of-eight design and a 3 mm baseline. MIA recordings were performed in a simpler electrically-shielded room. This work was performed using either single- or independent two-channel systems.

MCG and MEG measurements with 'flip chip' biomagnetometers were performed using a two-channel system with a signal and a reference channel, each of which were high-T_c DC SQUID biomagnetometers with 16 mm pickup loops. A two-channel bias-reversal DC SQUID electronics (Cryoton) unit enabled simultaneous operation of the magnetometers. The experiments were performed in standard MSRs in the Franz-Volhard Hospital (MCG measurements [53]) and the Institute of Neurosciences and Medicine, Forschungszentrum Jülich (MEG measurements [20, 54]). The shielding factor of the MSRs was about 10^4 at 50 Hz and about 10 at 0.1 Hz. The residual magnetic flux density in the middle of the MSRs was ~100 nT. A slow variation of the magnetic field in the middle of the MSRs was observed during daytime. The typical time constant of this drift was ~10 s with an amplitude of up to 5 nT. No active compensation of this low frequency environmental field noise was employed during the measurements. The feedback of the electronics was adjusted to follow the maximal changes of the magnetic field.

3.1. Application of high-T_c DC SQUID biomagnetometers for MCG

Cardiovascular diseases are the most common cause of early disability and death globally, contributing to about 17.3 million deaths/year (30% of all deaths in the year 2008), with a prognosis that this number will grow to more than 23.6 million deaths/year by 2030 [56]. The early detection of heart diseases has enormous potential benefits across the world because it opens up important possibilities to prevent or even reverse disease progression and to reduce its devastating impact on later life. The most common non-invasive test that is used to diagnose cardiovascular diseases is the electrocardiogram (ECG), which is ~50% accurate in the diagnosis of the leading contributor to cardiovascular disease: myocardial ischemia. Although MCG is rarely used, it is a non-invasive and contact-free technique that has impressive sensitivity (~91%) and specificity (~84%) for myocardial ischemia [57, 58]. The primary reason for the underutilization of MCG seems to be purely economic: the total running costs of existing low-T_c MCG systems are still too high for ordinary hospitals and clinics. This is true even though high quality MCGs can be generated in the absence of a bulky and expensive magnetically-shielded room [59]. The utilization of high-T_c DC SQUID biomagnetometers for MCG leads to a significant reduction in running costs. Although they still require magnetic shielding, long-term savings make them a cost-effective alternative to low-T_c MCG and perhaps even ECG.

Proof-of-principle MCG recordings with the two-channel high-T_c SQUID system were performed in the MSR of the Franz-Volhard Hospital [53]. At frequencies below 10 Hz, an increase in environmental noise, which was associated with the reduced shielding factor of the MSR, was observed. In the 10–30 Hz frequency range, magnetic field signals caused by building vibrations were also observed. By using analog subtraction of the signal output of the top magnetometer (reference channel) from the signal output of the bottom magnetometer (signal channel), the parasitic low frequency noise determined by the low frequency signal, vibration effects, and 50 Hz interference was reduced by more than an order of magnitude, such that NEMI levels of below 80 fT Hz^{-1} were reached at 1 Hz. The effective gradiometric resolution for the 'electronic' gradiometer was below 1 fT cm^{-1} Hz$^{-1/2}$) at frequencies of above 100 Hz and below 2 fT cm^{-1} Hz$^{-1/2}$) in the frequency range down to ~4 Hz. The white noise of the electronic gradiometer exceeded the noise of the individual magnetometers by a factor of approximately $\sqrt{2}$, in accordance with theoretical expectations.

MCG measurements were performed in the MSR with a volunteer having maximal peak-to-peak amplitude of ~30 pT for the magnetic signal of the heart. Both the magnetometer outputs and the electronic gradiometer signal were recorded simultaneously. The real-time result of subtraction of the reference channel is demonstrated in figure 7. A line frequency synchronous filter combined with a bandpass filter suppressed the residues of 50 Hz interference and its harmonics. The observed width of the noise trace of ~500 fT corresponds to an average NEMI of ~16 fT Hz$^{-1/2}$ in the measurement frequency bandwidth 0.03–125 Hz that covered the most significant frequency range of the heart signal.
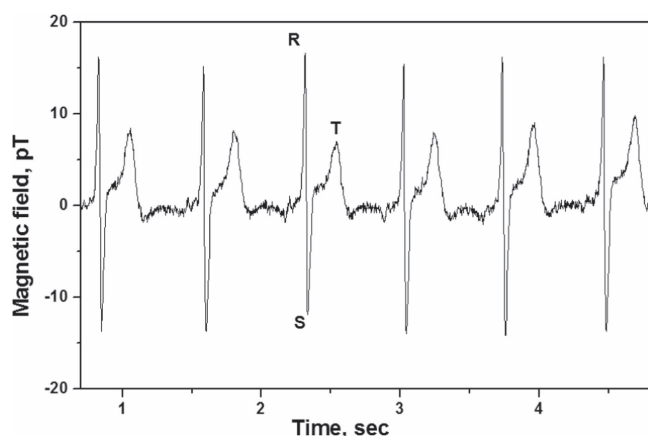
Figure 7. Real-time MCG measured by the electronic gradiometer. The frequency bandwidth was 0.03–125 Hz. Reprinted from [54], with the permission of AIP Publishing.
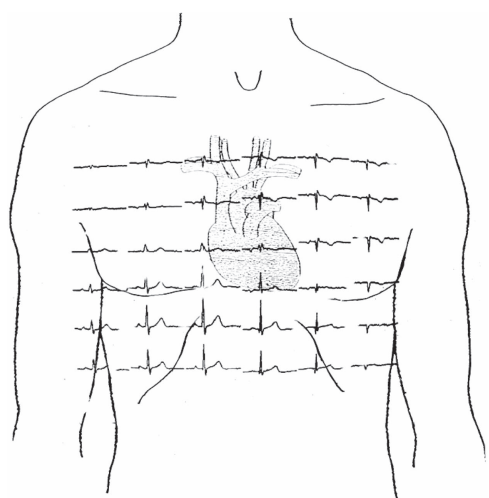

Figure 8. Signal plots over the thorax show averaged MCG signals measured by the electronic gradiometer at 6×6 grid positions. The recording time was 30 s per location.

The system's operating stability was demonstrated via measurements of MCG maps. Magnetic field measurements were carried out over a 6×6 square grid over the thorax with a distance of 4 cm between neighboring measurement positions in both directions (see figure 8). The total scan area was 20 cm × 20 cm. We used the simultaneously measured ECG channel as a trigger for averaging 30 s of MCG data at each measurement point. The low frequency ($\sim$0.1 Hz) drift of the magnetic field in the MSR and the effect of breathing caused some vertical offsets in the averaged differential signals, which can be seen in figure 7.

The total measurement time for all points was approximately 30 min. The magnetometers demonstrated stable operation and no change in noise performance over this time, allowing low noise 2D plots of the magnetic field distribution to be obtained. Equiinductional maps of magnetic field distribution were plotted on the basis of a two-dimensional interpolation at any moment of the heartbeat, as shown in figure 9. Interestingly, the magnitude of the MCG signal measured by the first order high-T_c electronic gradiometer was less attenuated for measurement points towards the periphery of the scan area, as compared with corresponding data from a low-T_c MCG system (based on second order gradiometer and Nb-wire pickup loops). This difference can be attributed to the increasing spatial filtering effect as the gradiometric order increases. The magnitude of the lead-field of a second order gradiometer decays more rapidly as a function of distance from the primary coil, when compared to that of a first order gradiometer with the same baseline.

3.2. Application of high-T_c DC SQUID biomagnetometers for MEG

Brain disorders represent approximately 35% of human diseases and lead to enormous suffering for patients and their families world-wide. It was estimated that the total cost of brain disorders was about €800 billion in 2010 for Europe alone [60]. Understanding the origin of brain diseases and dysfunctions is complicated by its extreme complexity. The human brain contains approximately 100 billion neurons at maturity, all with relative arrangements, mutual connections and functions that change over time. A variety of neuroimaging modalities exists, such as functional magnetic resonance imaging and positron emission tomography for the study of hemodynamics and metabolism, respectively, with high spatial resolution. In order to explore and understand spatio-temporal brain dynamics, electroencephalography (EEG) and/or MEG are used to study neuronal activity. Both modalities provide direct access to electrophysiological activity with a superb temporal resolution of about one millisecond and are non-invasive. Today, they are employed for neurological and psychiatric research and provide valuable information about the spatio-temporal organization of the human brain. In contrast to EEG, MEG is known to provide better spatial resolution, as it does not depend on heterogeneity in conductivity across different head tissues (e.g., skull, brain, cerebrospinal fluid, etc). However, when compared to MRI, the spatial resolution of MEG is worse and existing MEG technology needs further development to obtain reliable information from deeper brain areas with high spatial and temporal resolution. All commercial MEG systems are currently based on low-T_c SQUIDs, which require liquid helium for cooling to operate at 4.2 K. In contrast to liquid nitrogen, the availability of helium cannot be guaranteed for the future. Moreover, the ever-increasing cost of liquid helium threatens wide acceptance of MEG as a diagnostic tool in clinical practice and results in pressure to develop new sensors for MEG research that would be independent of liquid helium. While cryocoolers placed next to a MEG system may reduce or even eliminate helium consumption significantly, such an approach has yet to reach maturity in terms of, e.g., routine clinical utilization, with a significant problem being additional noise contributions.

In recent years, improvements in high-T_c SQUID technologies have shown that neuromagnetic signal recordings and results from post-processing obtained with a high-T_c SQUID system are in good agreement with those obtained from a commercial low-T_c MEG system [15, 20]. MEG measures magnetic field changes that originate from cortical
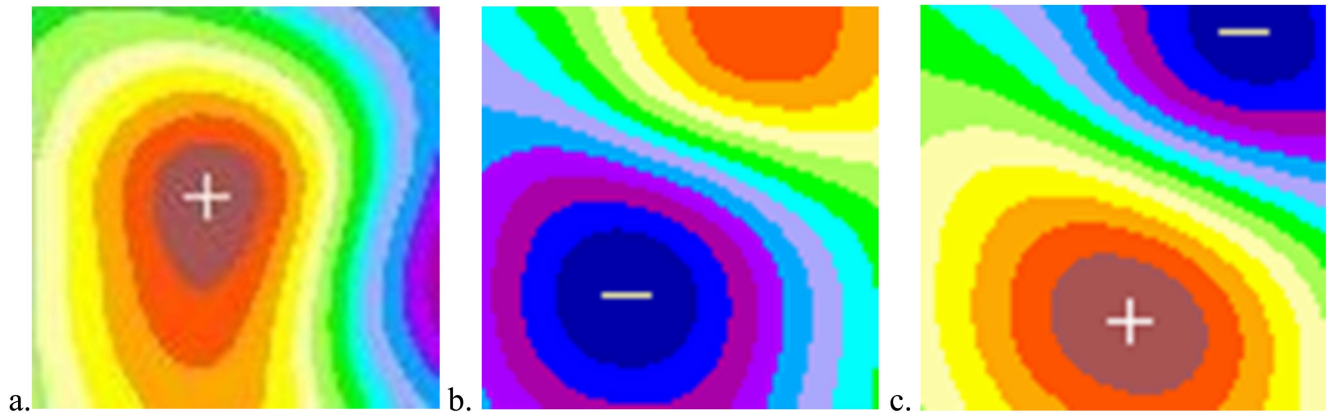
Figure 9. Magnetic field distributions over the 20 cm × 20 cm scan area measured at moments of the (a) R-, (b) S- and (c) T-peaks of the MCG.

activity with field strengths in the range of a few hundred fT. A typical NEMI for low-T_c MEG systems is about 4 fT Hz$^{-1/2}$, which is mainly limited by magnetic noise generated by thermal current fluctuations in the cryostat and the metal walls of the MSR and/or limited shielding of environmental noise by the MSR. For most routine MEG applications, a NEMI value of <10 fT Hz$^{-1/2}$ in the frequency range 1 Hz–1 kHz is sufficient and can be provided by high-T_c DC SQUID biomagnetometers. These circumstances have justified our proof-of-principle MEG recordings using high-T_c DC SQUID biomagnetometers, whose NEMI values are on that level [20, 54]. Importantly, our results indicate that the sensitivity of high-T_c SQUIDs is ready for MEG source analysis [54].

In the study reported in [13] (see figure 10), MEG measurements of spontaneous brain activity were performed in the MSR formerly located at Imego AB in Gothenburg. Two of the 'direct-coupled' magnetometers were housed in separate cryostats. The head-to-sensor distance was estimated at ∼1 mm for both channels. We studied the visual alpha (8–12 Hz) and sensorimotor alpha/mu (10–14 Hz) spontaneous brain rhythms via simultaneous single-shot recordings from O2 (visual/back right) and C4 (sensorimotor/right side) positions of the head with respect to the 10–20 coordinate system [61]. Both rhythms are well understood resting state neural oscillations, whose magnitudes are maximal when one is relaxed but alert. Visual alpha is strongest when the eyes are shut, while sensorimotor alpha/mu is strongest when there is a lack of both sensory input and motor control. Opening of the eyes suppresses visual alpha, whereas touch sensation and voluntary movement suppresses sensorimotor alpha/mu. Hand relaxation and flexure/closure were selected for modulating sensorimotor alpha/mu because the hand region occupies a large part of the sensory and motor cortices, thereby providing clear signals for recordings. The recording shown in figure 10 was 64 s long. During the first 32 s, the subject sat with open eyes and relaxed hands. After 32 s, the subject was verbally instructed to simultaneously close his eyes, flex his hands and hold that state for the remaining 32 s of the recording.
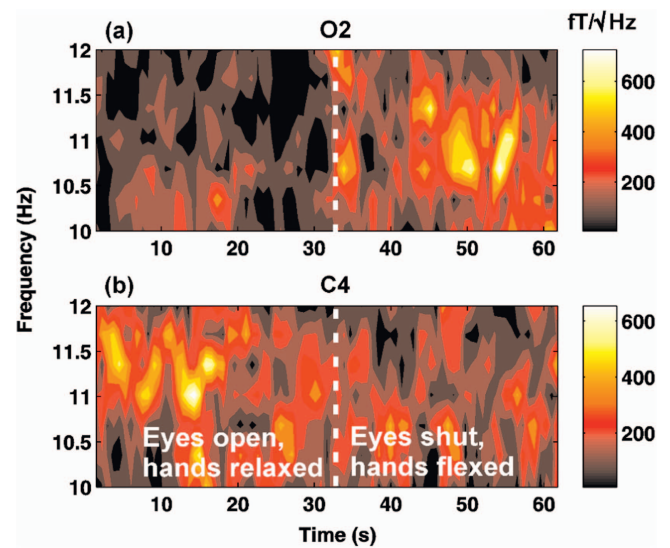

Figure 10. Time–frequency spectrograms of two-channel single-shot/un-averaged high-T_c SQUID biomagnetometer recordings of the modulation of neural oscillations. Adapted from [13], with the permission of AIP Publishing. (a) The channel placed at O2/ backside of the head records noise for the first 32 s of the recording, as the visual alpha signal is suppressed while the subject has open eyes. Upon closing of the eyes at 32 s and thereafter, clear alpha-band spontaneous brain rhythm activity is evident. (b) The channel placed at C4/side of the head (roughly over the sensorimotor cortex) records clear alpha/mu-band spontaneous brain rhythm activity as the subject sits with relaxed hands. Upon flexing/closing of the hands, this alpha/mu-band activity is suppressed below the noise floor of the recording.

Time–frequency analysis (TFA) was applied to both raw biomagnetometer recordings. A boxcar window binned the data with a step size of 0.7 s and an epoch width of 3 s. Each epoch then underwent an FFT. Alpha/mu rhythms typically appear at 8–12 Hz, the specific peak frequency of which is subject-specific. Figure 10 shows spectrograms for the subject, whose alpha/mu rhythms peaked at around 11 Hz. As expected, the visual alpha wave signal recorded at O2/the back of the head is weak when the subject had open eyes and is strong upon closing them. The simultaneously-recorded C4/side of the head channel provides evidence of sensitivity

to the sensorimotor alpha/mu rhythm, as the activity in that frequency range, while the subject is relaxed, is attenuated upon flexure/closer of the hands (also as expected). Despite the relatively high NEMI values of the simple single-layer 'direct-coupled' bicrystal-based JJ DC SQUID technology, this experiment demonstrated clear sensitivity to spontaneous brain activity with single-shot SNR levels of greater than 5.

In the studies reported in [20, 54], all MEG measurements were performed in the MSR of the Institute of Neurosciences and Medicine, Forschungszentrum Jülich, using both the high-T_c DC SQUID measurement system and the commercial 248 channel low-T_c MEG system 'Magnes$^\copyright$ 3600 WH' 4D-Neuroimaging. The analog output from the high-T_c system was connected to a 16-bit analog-to-digital converter port available on the low-T_c system with a sampling rate of 678 Hz and processed together with the signals from the low-T_c magnetometers. The NEMI of the high-T_c system was $\sim$5 fT Hz$^{-1/2}$ with the high-T_c magnetometer operating at 77 K in a cylindrical superconducting shield and $\sim$7 fT Hz$^{-1/2}$ (white noise level) at 77 K within the MSR. The low-T_c system had a NEMI of $\sim$5 fT Hz$^{-1/2}$ with the low-T_c SQUID operating at 4.2 K in the MSR. The head-to-sensor distances were about 15 mm and 19 mm for the high-T_c and low-T_c systems, respectively.

In 2014, the first successful source localization of neuromagnetic evoked responses was demonstrated using a single channel high-T_c SQUID [54]. In addition, TFA on resting state brain activity from visual areas revealed similar power spectral densities of spontaneous activity when compared to a commercial full-head low-T_c SQUID MEG system. A single subject (male, age 51, right handed) volunteered for both MEG experiments.

In order to investigate whether time–frequency-dependent oscillations recorded with a high-T_c SQUID system resemble those from a commercial low-T_c SQUID system, resting state brain activity was recorded in the same subjects with and without eyes closed using both high-T_c SQUID and low-T_c SQUID systems [54]. For the high-T_c SQUID measurements, spontaneous activity was recorded over the right occipital cortex. Neuromagnetic field changes were recorded continuously for 3 min with blocks of open/shut eyes for about 10 s, while the subject was asked (verbally) to open or close his eyes. The beginning of each block was documented by a change in the trigger code.

TFA was applied to spontaneous data recorded with the high-T_c and low-T_c SQUID systems using one channel located over the right occipital area of the subject. A total of nine epochs of 7 s duration were used to compute an average spectrogram, while all spectrograms were normalized to have unit variance prior to analysis for comparison between the low-T_c and high-T_c SQUID systems. In figure 11, clear changes in alpha power (8–12 Hz) are evident in both measurements using the low-T_c and high-T_c SQUID MEG systems. TFA of both data sets revealed spectrograms showing synchronization (increased power) and desynchronization (decreased power) of alpha rhythm upon closing and opening of the eyes, respectively, as expected.

For comparison between the low-T_c and high-T_c SQUID based power spectral densities, the MEG signals from both systems were normalized to unit variance prior to analysis. The peak-to-peak amplitude of the signal detected using the high-T_c system was slightly lower ($\sim$500 fT) than the peak-to-peak amplitude of the signals shown in figure 10 due to the larger sensor-to-scalp standoff for the 16 mm flip-chip sensors. However, the SNR in the case of the flip-chip sensors is higher due to lower NEMI values of the sensors.

The experiments described above showed that the signal dynamics and power recorded using high-T_c SQUID sensors resemble those recorded using low-T_c MEG systems. However, in order to test and compare results between sensor technologies, the same brain signals need to be recorded from various positions around the source of interest (i.e., a given brain activation). This is trivial using conventional full-head MEG systems, whose sensors surround the head, but is a challenge when only one (or a few) high-T_c SQUID biomagnetometers are available. We developed a protocol for efficient benchmarking of single (or a few) channel magnetometers versus conventional MEG sensor technology. The protocol, which is detailed in [15], includes obtaining a recording using a standard MEG system, source localization based on that data, forward projection of the magnetic field generated by the source to the head surface, and recordings with the high-T_c SQUID biomagnetometer at head locations where the projected magnetic field magnitude is maximal. We also included EEG recordings (the magnitudes of which are maximal at positions on the head that are rotated by 90° with respect to the magnetic field maxima and therefore easily accessible) during all MEG sessions for assessing the stability of the activations.

We compared the low-T_c SQUIDs within the Elekta Neuromag TRIUX system (102 magnetometers with a 21 mm × 21 mm pickup loop and 1–5 fT Hz$^{-1/2}$ magnetic field resolution at 4.2 K and 10 Hz) to one of the 'direct-coupled' high-T_c SQUID biomagnetometers (9 mm × 9 mm pickup loop and $\sim$40 fT Hz$^{-1/2}$ magnetic field noise at 77 K and 10 Hz). We selected the sensory N20m component induced by electrical stimulation of the median nerve (at the wrist) and the auditory P100m component induced by 1 kHz tones because both of these activations are known to be robust and to show little habituation. The recordings shown in figure 12 were performed inside the MSR at the Karolinska Institute NatMEG center in Stockholm. Low-T_c (blue) versus high-T_c (red) SQUID recordings were performed at the positions of maximal MEG signals. These positions are different for the low-T_c and high-T_c SQUID recordings because the sensor-to-scalp standoff is $\sim$40 mm for the low-T_c system and $\sim$5 mm for the high-T_c system. The difference between the positions of the sensors is the reason for the difference between the characteristic features of the MEG recordings. Figure 12 shows that for the auditory evoked fields the signal obtained using the high-T_c system is stronger than the auditory evoked field signal obtained using the high-T_c system by a factor 2.6–2.9. In the case of a somatosensory evoked field, the gain is between 3.4 and 4.2. Further experimental details can be found in [15].
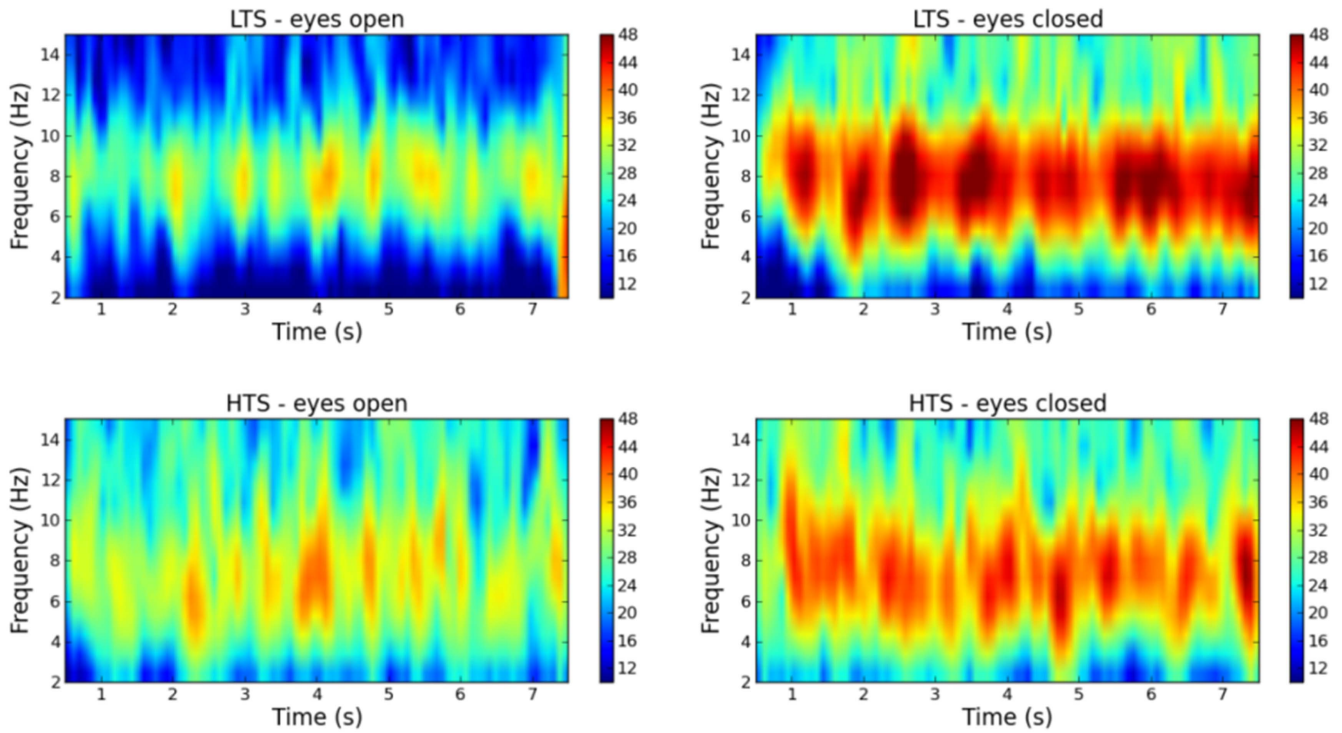
Figure 11. Time frequency analysis of alpha-band spontaneous neural oscillations recorded above the right occipital area using a low-T_c SQUID system (top row) and a high-T_c SQUID system (bottom row) from one subject with eyes opened (left column) and closed (right column). For both systems, the spectrograms show enhanced alpha activity during time periods of eyes closed, while desynchronization of the alpha rhythm is evident during recordings with open eyes. For comparison between the low-T_c and high-T_c SQUID based power spectral densities, the MEG signals from both systems were normalized to unit variance prior to analysis. Reprinted from [55], with the permission of AIP Publishing.
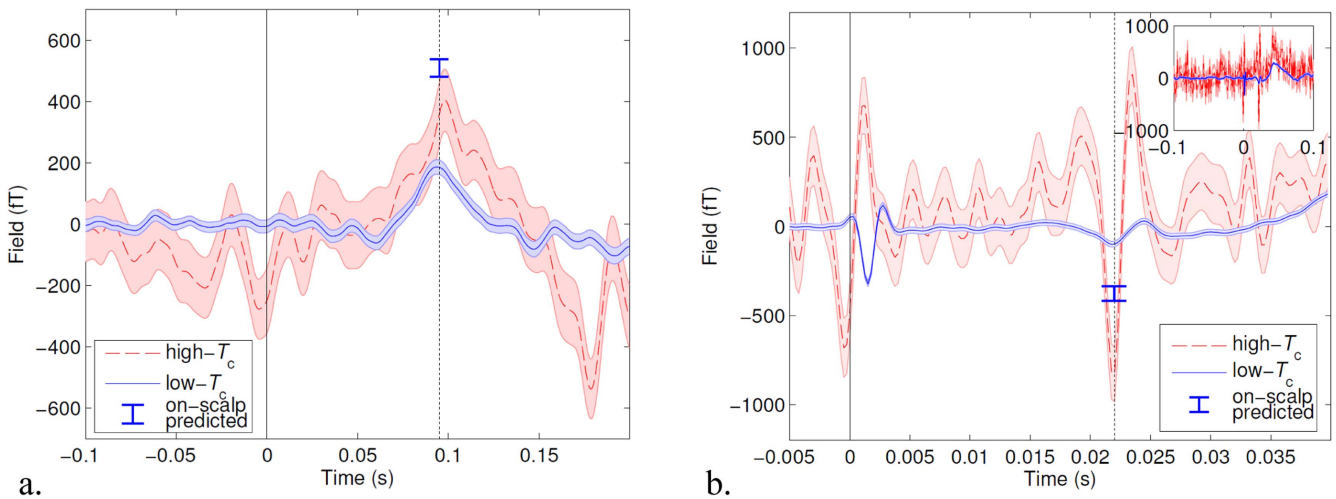

Figure 12. Low-T_c (blue) versus high-T_c (red) SQUID recordings of the (a) auditory P100m and (b) somatosensory N20m activations. © 1969 IEEE. Adapted, with permission, from [15]. Blue bars indicated the expected field magnitude of the activations based on the expected gain in signal available when recording the neuromagnetic field at the scalp surface (i.e., with high-T_c SQUIDs), in comparison to a few cm away (i.e., with low-T_c SQUIDs). For the auditory evoked fields, the expected gain was a factor of 2.6–2.9. The magnitude of the high-T_c recording is just below this range for the positive lobe of the field (pictured), and just above it for the negative lobe (not pictured). In the case of the somatosensory evoked field, the high-T_c signal significantly exceeds the expected gain of 3.4–4.2 for both the negative (pictured) and the positive (not pictured) lobes.

A more comprehensive way to test and compare results obtained using high-T_c SQUID biomagnetometers versus conventional low-T_c MEG systems is to perform recordings from many head positions, such that source localization can be implemented using both sensor types. In [54], auditory evoked magnetic field responses were recorded in separate

runs and at 16 different locations above the left temporoparietal area (the region surrounding the auditory cortex) using both the low-T_c and the high-T_c MEG system. These measurements were performed in Jülich using a single channel high-T_c MEG system equipped with 16 mm flip-chip high-T_c DC SQUID biomagnetometers and a 248-channel low-T_c MEG system.

The measurement locations for the high-T_c SQUID system were defined by the location of the electrode position of the EEG cap (EASYCAP GmbH, Berlin, Germany), which the subject was wearing without EEG electrodes (see figure 5(a)). In order to define the subject's head, a coordinate system, including the coordinates of the electrode locations, the head surface and the electrode position of the EEG cap, were digitized using a 3D digitizer from Polhemus (Polhemus, 3Space/Fastrak, USA). The cylindrical liquid nitrogen dewar from the high-T_c system was positioned above 16 different locations of the electrode mountings of the EEG cap. With the EEG cap placed between the head and the cryostat (see figure 5(a)), the distance between the subject's head and the pickup coil was approximately 20 mm for all measurement locations.

During the experiments, 300 binaural stimulations were presented randomly (SOA[6] 1.8 ± 0.3 s), while neuromagnetic brain responses were recorded. The intensity of the auditory click tones was adjusted to the comfortable hearing level of the subject. All MEG measurements were performed with the subject in the supine position. The neuromagnetic activity was continuously recorded with a sampling rate of 678.17 Hz and a bandwidth ranging from DC to 200 Hz. All tone onsets were shifted by -19 ms due to the delay of the sound delivery system, while an additional delay of 6 ms was subtracted from the high-T_c SQUID measurement due to the constant delay in the high-T_c SQUID readout electronics. For comparison, responses to auditory stimulation from the entire brain were acquired using a whole-head MEG system equipped with 248 low-T_c SQUID magnetometers.

A specific analysis procedure was implemented with respect to source localization of the auditory-evoked field recorded by the high-T_c SQUID system. The identification of unusually large amplitudes (e.g., due to artifacts) in the signal of the high-T_c and low-T_c SQUID recordings was performed on the raw data by using a peak-to-peak measure applied to the full data set with a sliding window of length 200 ms. A bandpass filter ranging from 3 to 30 Hz as well as a notch filter at the power line frequency of 50 Hz and harmonics were applied. Trials around the stimulus onset were defined with 1 s post- and 400 ms pre-stimulus. The number of trials included for further analysis after discarding those with artifacts or unusually large amplitudes was, on average, 293 and 294 for the low-T_c and high-T_c SQUID recordings, respectively. Finally, all trials were averaged based on stimulus onset time. For comparison of the results from source analysis between the two systems, positions from the high-T_c SQUID measurements were aligned to low-T_c SQUID sensors that best matched the location of the high-T_c SQUID recording.

A dipolar field pattern can be seen in both the low-T_c SQUID and the high-T_c SQUID topographic field maps (see insets over the head sketches in figure 13). Isocontours of the evoked fields are shown for a peak latency of about 87 ms after the stimulus onset. The field distribution measured using the high-T_c SQUID system at 16 different positions resembles the field map of the low-T_c SQUID system in this area and clearly covers the zero-field-line that roughly indicates the location of the source. The left part of figure 13 shows MEG signal averages from the left hemisphere in response to auditory stimulation. The top panel shows a signal average using 50 channels over the left temporal cortex, as obtained by the whole head low-T_c SQUID magnetometer system (blue). The bottom panel shows signals from the same subject obtained using a single high-T_c SQUID at 16 different positions (red). The time range highlighted in gray was used for source analysis. The traces obtained from both the high-T_c and the low-T_c systems demonstrate similar SNR, despite the $18\times$ difference in the operating temperatures of the sensors.

The single dipole fit algorithm, as provided by the 4D-Neuroimaging MEG system, was applied to localize the sources of the dipolar fields that were recorded [62]. Analysis of the high-T_c SQUID measurements included MEG signals from the 16 different positions (figure 13). For analysis of the low-T_c SQUID recordings, the system pre-defined group of 50 channels covering the left temporoparietal area was used. The larger number of channels was kept for source analysis of the low-T_c system data because it serves as a reference.

Estimation of the dipolar source was performed using a time window of 50 ms between 60 and 110 ms. The dipole with the best goodness-of fit value from the low-T_c SQUID measurement was chosen for comparison and was found to be maximal 104 ms after stimulus onset. Analysis of the high-T_c and low-T_c SQUID recordings revealed a dipolar source with the same latency as expected (figure 14). The location of this source, as determined using the single high-T_c SQUID system, is in very good agreement to that determined using the low-T_c system. Both the location and the direction of the source estimations are comparable. The high-T_c SQUID source analysis revealed a displacement of only 7 mm compared to the results obtained using the low-T_c SQUID system [54].

A possible further development of the high-T_c MEG system is to use several ten-channel systems with individual cryostats. Each cryostat can then enclose, for example, seven signal channels and three reference channels. A photograph of such a cryostat and a sketch of a ten-channel MEG system that is under construction are shown in figures 15(a) and (b), respectively. The $\sim$11 l commercial cryostat from Tristan Technologies Inc. (originally intended for liquid helium) holds liquid nitrogen for more than two weeks with an evaporation rate of approximately 0.8 l d^{-1}. A liquid nitrogen evaporation rate of below 0.3 l d^{-1} is expected for a cryostat of similar size that is specifically designed to hold liquid nitrogen. Such a seven-signal-channel system configuration will be used for the investigation of a region of human brain that is related to a specific functional activity.
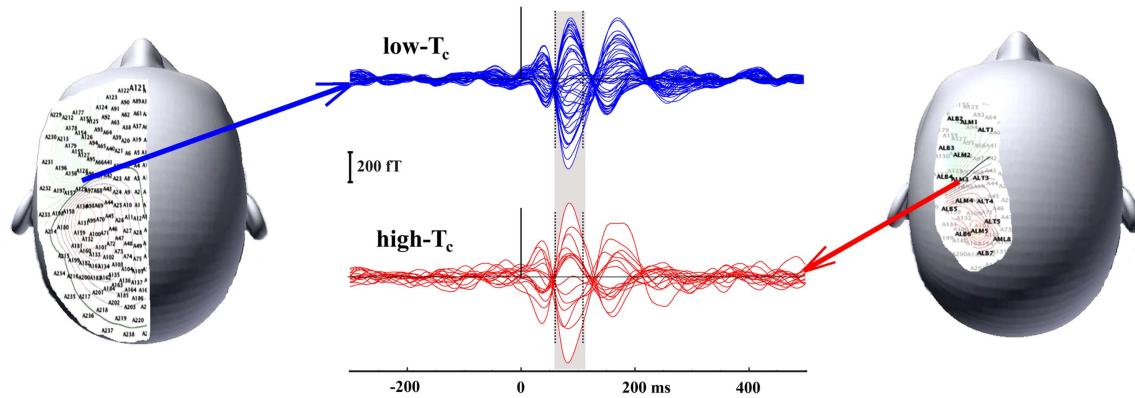
---

[6] Stimulus onset asynchrony (SOA) describes the average time from one stimulus to the other, whereas onset times are randomized.

Figure 13. Comparison of auditory evoked MEG averaged signals acquired at a similar location over the left hemisphere using low-T_c (50 positions, blue, upper curve) and high-T_c (16 positions, red, lower curves) SQUID systems. The time range highlighted in gray was used for source analysis. Adapted from [55], with the permission of AIP Publishing.
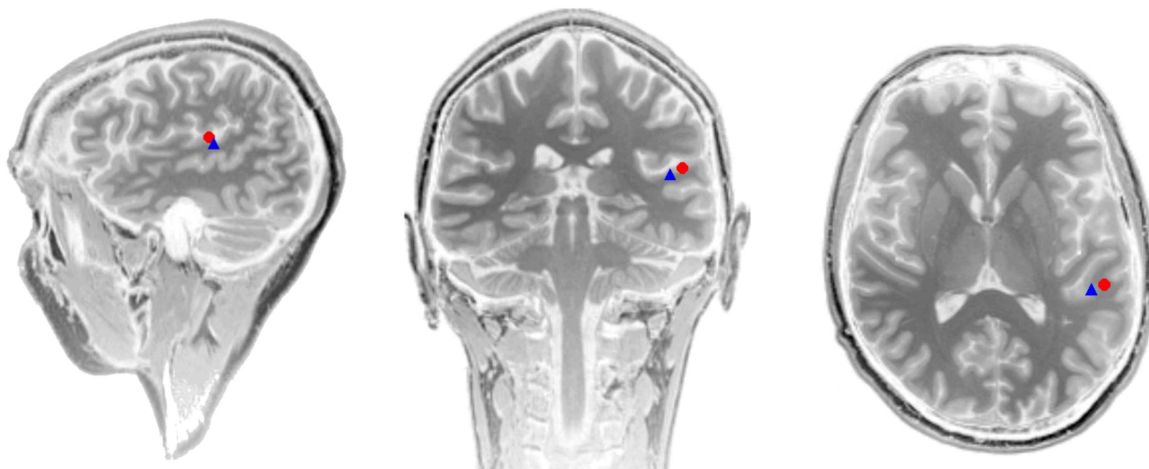

Figure 14. Results from source analysis of auditory evoked neuromagnetic field responses, as recorded using high-T_c SQUID (red circle) and low-T_c SQUID (blue triangle) systems. The location of the dipolar source from the high-T_c SQUID system (red) is, as expected, in the region of the left primary auditory cortex and is in very good agreement with source analysis from data recorded using the low-T_c SQUID system (blue). Middle image reprinted from [55], with the permission of AIP Publishing.
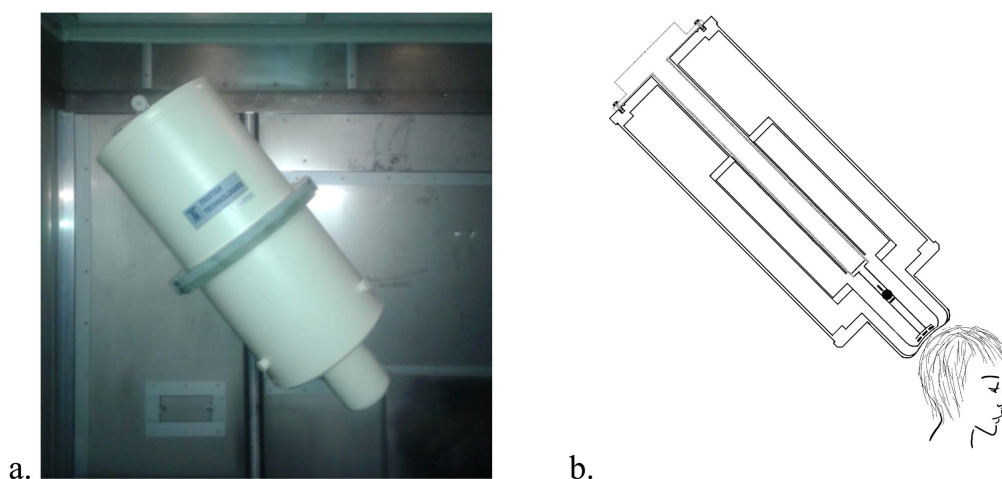

Figure 15. (a) Photograph of a cryostat intended for a ten-channel MEG system fixed on an adjustable cryostat holder in a magnetically-shielded room in the Peter Grünberg Institute, Forschungszentrum Jülich GmbH. (b) Sketch of a ten-channel MEG system that is under construction.
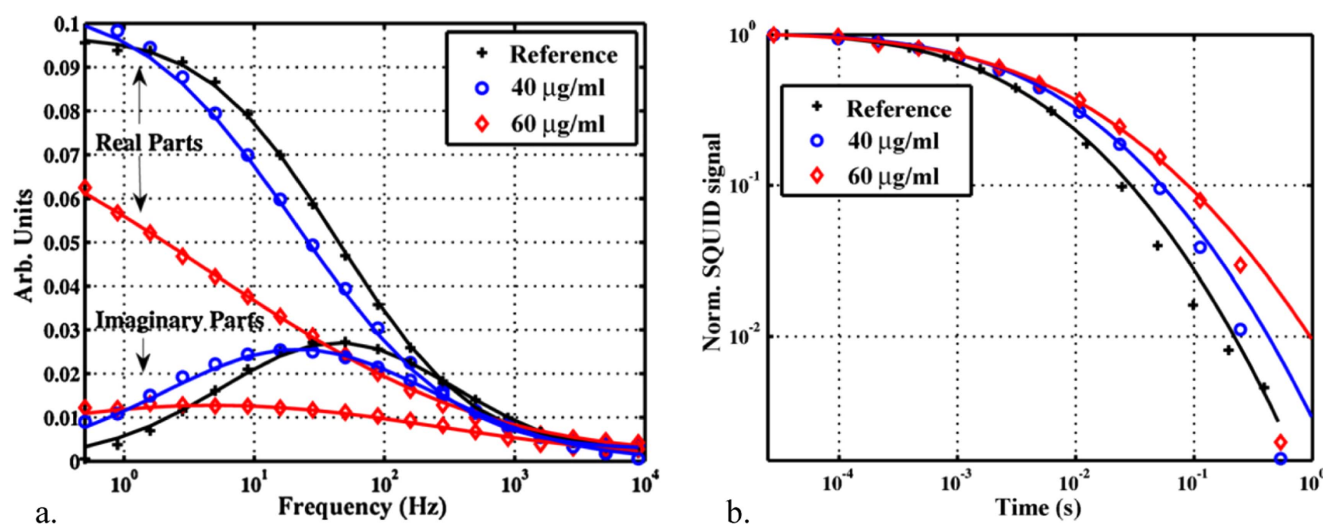
Figure 16. (a) Frequency and (b) time domain measurements of MNP Brownian relaxation dynamics, as recorded using direct-coupled high-T_c SQUID biomagnetometers. As the concentration of analyte increases, the average Brownian relaxation slows, shifting the peak of the imaginary part of the complex susceptibility (a) down in frequency and (b) slowing the relaxation dynamics in the time domain. Reprinted from [56], Copyright 2010, with permission from Elsevier.

3.3. High-T_c DC SQUID biomagnetometers and MNPs

Ferrimagnetic crystals of magnetite (Fe_3O_4) that are below 100 nm in size occur naturally in bacteria, protists, animals and humans due to biomineralization (see [1, 63, 64] and references therein). High-T_c DC SQUIDs can easily resolve the magnetic fields produced by the motion of even a single living magnetotactic bacterium [65]. Functionalized MNPs of magnetite are used for the magnetic hyperthermia treatment of cancer and serve for targeted drug delivery to increase drug concentration in tissues or because they can be transported through the vascular system and concentrated at a particular point of the body with the aid of a locally applied magnetic field [1, 66–68]. Antibody-conjugated MNPs are able to find (*in vivo* and/or *in vitro*) proteins that are specific for cancer, Alzheimer, and Parkinson diseases, to serve as their magnetic biomarker, and to diagnose these diseases at an early stage with the help of high-T_c SQUIDs [69–71].

Chalmers has developed a one-step biomolecular assay that is based on sensitivity to changes in fluid-suspended MNP Brownian relaxation dynamics in the frequency and time domains [55]. For this experiment, biofunctionalized multi-core particles containing single domains of $CoFe_2O_4$ (Chemicell GmbH) with a median hydrodynamic radius of 50 nm were used. The MNPs were functionalized with streptavidin with biotinylated monoclonal antibodies. A prostate-specific antigen (PSA) assay was targeted as a model system. MNPs can bind 80 pmol of biotinylated protein per mg of MNPs, which corresponds to approximately 30 PSA10 molecules per MNP. PSA10 is a monoclonal antibody for PSA and acts as a capturing antibody for the specific targeting of PSA. In this study, a 'direct-coupled' high-T_c DC SQUID gradiometer with balance 93, spectral flux noise 4.5 $\mu\Phi_0$ Hz$^{-1/2}$ at 1 kHz, and a gradient resolution of $\sim$2.1 pT cm^{-1} Hz$^{-1/2}$) was used [26]. The same ILK Dresden cryostat was used as in the Chalmers 'direct-coupled' MEG experiments. For such measurements of fluid-suspended

MNPs, proximity between the sensor and the room temperature environment is particularly powerful. The size of the gradiometer (baseline 3 mm) was small enough to be used effectively without magnetic shielding, while having sensitivity to extremely small volumes (as little as 1 μl) of fluid-suspended MNPs. Despite the size of this volume, the roughly 1×10^8 MNPs have a total surface area of several square centimetres. This is significantly larger than standard well-based biomolecular assays, whose binding areas (i.e., 'sensing areas') are typically no larger than 1 cm^2. The estimated MNP content sensitivity of $\sim$50 ng Hz$^{-1/2}$ ($\sim$1.1 $\times$ 10^8 MNPs) was limited by the flux sensitivity of the gradiometer of $\sim$100 $\mu\Phi_0$ Hz$^{-1/2}$ at 2 Hz. Figure 16 shows the sensitivity of the measurements to varying analyte concentrations as surface binding events slow the MNP relaxation. The samples were measured in the frequency domain (figure 16(a)) using AC-susceptometry at different frequencies (frequency dependence of the complex susceptibility) and in the time domain (figure 16(b)) using magnetorelaxometry and a pulsed magnetic field. As the concentration of analyte increases, the average Brownian relaxation slows, shifting the peak of the imaginary part of the complex susceptibility (figure 16(a)) down in frequency and slowing the relaxation dynamics in the time domain (figure 16(b)).

The minimum volume of the liquid containing the MNPs required to detect a signal was about 0.3 nl at a particle number density of 1.8 $\times$ 10^{15} g^{-1}. This volume corresponds to 2.2 $\times$ 10^7 MNPs with a total magnetic moment of 0.3 pA m^2 and an average magnetic dipole moment per particle of 4.8 $\times$ 10^{-22} A m^2. The observed remnant signal was probably due to alignment of the magnetic moments of the MNPs in the Earth's magnetic field. The estimated ultimate biomolecular sensitivity for this measurement system is $\sim$8 $\times$ 10^8 molecules in a 2 μl sample volume, corresponding to a density of MNPs of $\sim$100 ng ml^{-1}. This measurement system can be

adapted to other disease markers, for which trapping antibodies are available.

4. Discussion

Despite the discovery of high temperature superconductors by Bednorz and Müller in 1986 [72] and subsequent developments of high-T_c SQUIDs that are capable of operation at liquid nitrogen temperature, all commercial MCG and MEG devices are still presently based on low-T_c SQUIDs that require liquid helium for operation at 4.2 K. Nevertheless, sensors that function at liquid nitrogen temperature (77 K) have significant economic and technical advantages. Both earlier and more recent publications have reported successful recordings of MCG and MEG that utilize single-channel or multi-channel systems [73–78] based on direct-coupled high-T_c SQUID magnetometers with bicrystal JJs. MCG systems that are based on direct-coupled high-T_c SQUIDs demonstrate sufficiently high SNR in MSRs because typical MCG signals are relatively large. Outside MSRs, the operation of high-T_c SQUID magnetometers is severely degraded due to electromagnetic interference, which leads to instability and too low SNR of MCG signals in most locations. Electromagnetic interference can be avoided in the case of well-balanced second order gradiometric low-T_c MCG systems that are able to operate well outside MSRs [59]. Direct-coupled high-T_c SQUID magnetometers also have advantages for applications to MNPs in bioassays and magnetic label imaging, where the sample can be positioned very close to the outer wall of the cryostat. All high-T_c and low-T_c MEG systems need MSRs for their low-noise operation. Direct-coupled high-T_c SQUID magnetometers are able to detect MEG signals and can be placed very close to the scalp. However, the common understanding has traditionally been that the noise level of direct-coupled high-T_c SQUIDs is too high, e.g., to localize neuromagnetic brain activity, which typically occurs several cm deep inside the head. Flip-chip high-T_c SQUIDs produced in the 90 s were made with sizes of pickup loops of below 10 mm and NEMI values down to about 10 fT Hz$^{-1/2}$ at 77 K and frequencies above 1 kHz [16, 17], which is beyond the frequency range of MEG measurements.

Very recently, significant improvements in the design and manufacture of 16 mm flip-chip high-T_c SQUIDs with NEMI down to about 4 fT Hz$^{-1/2}$ at 77 K and frequencies of below 100 Hz were reported by the Jülich group [20, 79], indicating that it will be possible to use high-T_c SQUIDs for MEG applications. In a series of tests, the suitability of this new sensor technology to go beyond just the detection of spontaneous and evoked brain signals was explored. As such, it was aimed to use the flip-chip high-T_c biomagnetometers to provide a SNR that is sufficient for TFA and source localization of evoked brain activity. The results confirm that the new high-T_c SQUID technology can be utilized for MEG studies that include time–frequency and even source analysis. The advantage of using SQUIDs is their combination of high sensitivity (a few fT Hz$^{-1/2}$), large frequency bandwidth

(a few MHz [11]) and large dynamic range (>100 dB) if flux counting electronics is used, as well as relatively small crosstalk values. Crosstalk between sensors is critical for accurate representation of the spatial distribution of the magnetic field in both MCG and MEG. The magnetic field of the feedback coil decays as a function of its area $\sim A^{-3/2}$. The feedback signal for SQUIDs can be injected directly into the $A \sim 0.01$ mm^2 area of the SQUID loop. In the case of atomic magnetometers, the feedback coil should provide a homogeneous field over a cross-sectional area of ~ 300 mm^2 [9]. As such, the radius of equivalent crosstalk (i.e., the distance between sensors with equal crosstalk) for atomic magnetometer sensors can be as much as $\sim 5 \times 10^6$ larger than for SQUIDs. While all SQUIDs require low operating temperatures, high-T_c SQUIDs are far less limited by this restriction when compared to low-T_c SQUIDs.

Crosstalk and cooling aside, the primary advantage of using high-T_c SQUIDs for MEG and MCG is that long-standing experience in SQUID sensor, readout electronics, and dewar technology exists. Therefore, a potential shift from low-T_c to high-T_c SQUID technology is expected to be straightforward. Theoretically, the field resolution of high-T_c SQUID magnetometers can be improved further. A magnetic field resolution of well below 1 fT Hz$^{-1/2}$ at 77 K should be achievable by using electron beam lithography to pattern JJs, a dual SQUID layout, flux transformers with larger pickup loops, and liquid nitrogen pumped down to its triple point temperature of 63.15 K. There is also the possibility of extending the current technology further for the preparation of multilayer high-T_c DC SQUID planar gradiometers of first or second order on single crystal MgO substrates that are up to ~ 10 cm long. Such a development can be useful for MEG recordings where the magnetically shielded environment is relatively weak. High-T_c SQUIDs with novel graphoepitaxial step-edge junctions can be fabricated at lower cost and with improved reproducibility, when compared to the previously widely used bicrystal technology. Perhaps more importantly in terms of biomagnetometry, high-T_c SQUIDs also enable a significant reduction in distance between the pickup coil and the subject's head (from ~ 20 to ~ 3 mm or less) or chest, leading to improved MEG/MCG recordings when compared to the state-of-the-art.

5. Summary

In summary, high-T_c SQUID biomagnetometers have been shown to demonstrate their usefulness for the two most important biomedical applications: MCG and MEG. The results encourage and pave the way for the development of multi-channel high-T_c SQUID based MCG and MEG systems. In the long term, we expect low-T_c DC SQUIDs to be replaced by graphoepitaxial step-edge-junction-based high-T_c technology for many applications, including future biomagnetic systems. Such an upgrade would make future multichannel systems independent of helium supplies, more user-friendly, and perhaps even more sensitive than what is available today. For example, we expect that a helium-free MEG system may save up to about

100 000-€ yr^{-1} due to a reduction in the operating cost for each system. More importantly, the availability of liquid nitrogen is guaranteed, in contrast to liquid helium. High-T_c SQUIDs with novel graphoepitaxial step-edge junctions [20, 22, 29, 31] promise better superconducting parameters, better reproducibility and lower cost when compared to previously widely used high-T_c SQUIDs with less available bicrystal JJs. When compared to other sensor technologies, the advantage of using SQUIDs is their combination of high sensitivity (a few fT Hz$^{-1/2}$), frequency bandwidth (a few MHz [11]) and dynamic range ($>$100 dB), as well as relatively small crosstalk values.

Acknowledgments

ORCID

M I Faley https://orcid.org/0000-0003-2768-2796
J Dammers https://orcid.org/0000-0003-1526-6592
J F Schneiderman https://orcid.org/0000-0002-4441-2360
D Winkler https://orcid.org/0000-0001-8332-3742
V P Koshelets https://orcid.org/0000-0002-1563-1257
N J Shah https://orcid.org/0000-0002-8151-6169
R E Dunin-Borkowski https://orcid.org/0000-0001-8082-0647

References

[1] Andrä W and Novak H (ed) 2007 *Magnetism in Medicine. A Handbook* (Weinheim: Wiley)

[2] Clarke J and Braginski A I (ed) 2006 *The SQUID Handbook Vol 2: Applications of SQUIDs and SQUID Systems* (Weinheim: Wiley)

[3] Seidel P (ed) 2015 *Applied Superconductivity: Handbook on Devices and Applications* vol 2 (Weinheim: Wiley)

[4] Sander T H, Preusser J, Mhaskar R, Kitching J, Trahms L and Knappe S 2012 Magnetoencephalography with a chip-scale atomic magnetometer *Biomed. Opt. Express* **3** 981

[5] Johnson C, Schwindt P D D and Weisend M 2010 Magnetoencephalography with a two-color pump-probe, fiber-coupled atomic magnetometer *Appl. Phys. Lett.* **97** 243703

[6] Sheng D, Li S, Dural N and Romalis M V 2013 Subfemtotesla scalar atomic magnetometry using multipass cells *Phys. Rev. Lett.* **110** 160802

[7] Iivanainen J, Stenroos M and Parkkonen L 2016 Measuring MEG closer to the brain: performance of on-scalp sensor arrays *NeuroImage* **147** 542

[8] Boto E, Bowtell R, Krüger P, Fromhold T M, Morris P G, Meyer S S, Barnes G R and Brookes M J 2016 On the potential of a new generation of magnetometers for MEG: a beamformer simulation study *PLoS One* **11** e0157655

[9] Boto E *et al* 2017 A new generation of magnetoencephalography: room temperature measurements using optically-pumped magnetometers *NeuroImage* **149** 404

[10] Budker D and Romalis M 2007 Optical magnetometry *Nat. Phys.* **3** 227

[11] Ludwig C, Kessler C, Steinfort A J and Ludwig W 2001 Versatile high performance digital SQUID electronics *IEEE Trans. Appl. Supercond.* **11** 1122

[12] Halperin W P 2014 The impact of helium shortages on basic research *Nat. Phys.* **10** 467

[13] Öisjöen F, Schneiderman J F, Figueras G A, Chukharkin M L, Kalabukhov A, Hedström A, Elam M and Winkler D 2012 High-T_c superconducting quantum interference device recordings of spontaneous brain activity: towards high-T_c magnetoencephalography *Appl. Phys. Lett.* **100** 132601

[14] Schneiderman J F 2014 Information content with low-versus high-T_c SQUID arrays in MEG recordings: the case for high-T_c SQUID-based MEG *J. Neurosci. Methods* **222** 42

[15] Xie M *et al* 2016 Benchmarking for on-scalp MEG sensors *IEEE Trans. Biomed. Eng.* accepted for publication **00871** 1–7

[16] Dantsker E, Ludwig F, Kleiner R, Clarke J, Teepe M, Lee L P, McN Alford N and Button T 1995 Addendum: low noise YBa$_2$Cu$_3$O$_{7-x}$–SrTiO$_3$–YBa$_2$Cu$_3$O$_{7-x}$ multilayers for improved superconducting magnetometers *Appl. Phys. Lett.* **67** 725

[17] Drung D *et al* 1996 Integrated YBa$_2$Cu$_3$O$_{7-x}$ magnetometer for biomagnetic measurements *Appl. Phys. Lett.* **68** 1421

[18] Faley M I, Poppe U, Urban K, Paulson D N, Starr T and Fagaly R L 2001 Low noise HTS dc-SQUID flip-chip magnetometers and gradiometers *IEEE Trans. Appl. Supercond.* **11** 1383

[19] Faley M I, Jia C L, Houben L, Meertens D, Poppe U and Urban K 2006 Meandering of the grain boundary and d-wave effects in high-T_c bicrystal Josephson junctions *Supercond. Sci. Technol.* **19** S195–9

[20] Faley M I *et al* 2013 High-T_c DC SQUIDs for magnetoencephalography *IEEE Trans. Appl. Supercond.* **23** 1600705

[21] Poppe U *et al* 1992 Low-resistivity epitaxial YBa$_2$Cu$_3$O$_7$ thin films with improved microstructure and reduced microwave losses *J. Appl. Phys.* **71** 5572–8

[22] Faley M I 2015 Reproducible step-edge Josephson junction Patent US 20150069331(published) and Patent EP 2834860 B1 (granted 30.12.2015)

[23] Gross R, Chaudhari P, Kawasaki M, Ketchen M B and Gupta A 1990 Low noise YBa$_2$Cu$_3$O$_{7-\delta}$ grain boundary junction dc SQUIDs *Appl. Phys. Lett.* **57** 727

[24] CRYOTON Co. Ltd, Solnechnaya Avenue 12, Troitsk, 142190, Moscow, Russia. http://europe.guide.ieeecsc.org/organization/cryoton-co-ltd

[25] ILK Dresden http://ilkdresden.de/en/project/cryostats-non-metallic-and-metallic/

[26] Öisjöen F, Magnelind P, Kalabukhov A and Winkler D 2008 High-T_c SQUID gradiometer system for immunoassays *Supercond. Sci. Technol.* **21** 034004

[27] Öisjöen F 2012 High-T_c SQUIDs for biomedical applications: immunoassays, magnetoencephalography, and ultra-low field magnetic resonance imaging *PhD Thesis* Chalmers University of Technology

[28] Gustafsson D, Lombardi F and Bauch T 2011 Noise properties of nanoscale $YBa_2Cu_3O_{7-\delta}$ Josephson junctions *Phys. Rev. B* **84** 184526

[29] Faley M I, Yu Slobodchikov V, Maslennikov Y V, Koshelets V P and Dunin-Borkowski R E 2016 High-T_c dual-SQUIDs with graphoepitaxial step-edge junctions *IEEE Trans. Appl. Supercond.* **26** 1600404

[30] Mitchell E E and Foley C P 2010 YBCO step-edge junctions with high I_cR_n *Supercond. Sci. Technol.* **23** 065007

[31] Faley M I, Meertens D, Poppe U and Dunin-Borkowski R E 2013 Graphoepitaxial Josephson junctions and DC SQUIDs *IEEE 14th Int. Superconductive Electronics Conf. (ISEC)* (IEEE Xplore Digital Library) pp 1–3

[32] Lam S K H and Gnanarajan S 2003 The investigation of transport properties on $Y_1Ba_2Cu_3O_{7-x}$ step edge junctions by ion beam etching *Physica* C **385** 466

[33] Clarke J 1996 SQUID fundamentals *SQUID Sensors: Fundamentals, Fabrication and Applications* (*NATO ASI Series E: Applied. Science* vol 329) ed H Weinstock (Dordrecht: Kluwer Academic) p 1

[34] Schmelz M, Stolz R, Zakosarenko V, Anders S, Fritzsch L, Roth H and Meyer H-G 2012 Highly sensitive miniature SQUID magnetometer fabricated with cross-type Josephson tunnel junctions *Physica* C **478** 77

[35] Ya Tzalenchuck A, Lindström T, Charlebois S A, Stepantsov E A, Zagoskin A M, Ivanov Z and Claeson T 2003 Feasibillity studies of ultra-small josephson junctions for qubits *IEEE Trans. Appl. Supercond.* **13** 948

[36] Faley M I, Poppe U, Urban K and Fagaly R L 2010 Noise analysis of dc-SQUIDs with damped superconducting flux transformers *J. Phys.: Conf. Ser.* **234** 042009

[37] Faley M I, Poppe U, Soltner H, Jia C L, Siegel M and Urban K 1993 Josephson junctions, interconnects and crossovers on chemically etched edges of $YBa_2Cu_3O_7$ *Appl. Phys. Lett.* **63** 2138

[38] Chukharkin M, Kalabukhov A, Schneiderman J F, Öisjöen F, Snigirev O, Lai Z and Winkler D 2012 Noise properties of high-T_c superconducting flux transformers fabricated using chemical-mechanical polishing *Appl. Phys. Lett.* **101** 042602

[39] Faley M I *et al* 2015 Integration issues of graphoepitaxial high-T_c SQUIDs into multichannel MEG systems *IEEE Trans. Appl. Supercond.* **25** 1601605

[40] Faley M I, Mi S B, Petraru A, Jia C L, Poppe U and Urban K 2006 Multilayer buffer for high-temperature superconductor devices on MgO *Appl. Phys. Lett.* **89** 082507

[41] Mi S B, Jia C L, Faley M I, Poppe U and Urban K 2007 High resolution electron microscopy of microstructure of $SrTiO_3/BaZrO_3$ bilayer thin films on MgO substrates *J. Cryst. Growth* **300** 478

[42] Matlashov A, Bakharev A, Zhuravlev Y and Slobodchikov V 1992 Biomagnetic multi-channel system consisting of several self-contained autonomous small-size units *Superconducting Devices and Their Applications* vol 64 ed H Koch and H Lübbig (Berlin: Springer) p 511

[43] Kalabukhov A, de Hoon E-J, Kuit K, Lerou P-P M, Chukharkin M, Schneiderman J F, Sepehri S, Sanz-Velasco A, Jesorka A and Winkler D 2016 Operation of a high-T_c SQUID gradiometer with a two-stage MEMS-based Joule–Thomson micro-cooler *Supercond. Sci. Technol.* **29** 095014

[44] Clarke J, Goubau W M and Ketchen M B 1976 Tunnel junction de SQUID: fabrication, operation, and performance *J. Low Temp. Phys.* **25** 99

[45] Drung D 2003 High-T_c and low-T_c dc SQUID electronics *Supercond. Sci. Technol.* **16** 1320

[46] Savo B, Wellstood F C and Clarke J 1987 Low-frequency excess noise in Nb–Al_2O_3–Nb Josephson tunnel junctions *Appl. Phys. Lett.* **50** 1757

[47] Koelle D, Kleiner R, Ludwig F, Dantsker E and Clarke J 1999 High-transition-temperature superconducting quantum interference devices *Rev. Mod. Phys.* **71** 631

[48] Koch R H, Clarke J, Goubau W M, Martinis J M, Pegrum C M and Harlingen D J V 1983 Flicker ($1/f$) noise in tunnel junction DC squids *J. Low Temp. Phys.* **51** 207

[49] Foglietti V, Gallagher W J, Ketchen M B, Kleinsasser A W, Koch R H, Raider S I and Sandstrom R L 1986 Low-frequency noise in low $1/f$ noise dc SQUIDs *Appl. Phys. Lett.* **49** 1393

[50] Burmistrov E V, Yu Slobodchikov V, Khanin V V, Maslennikov Y V and Snigirev O V 2008 Modulation SQUID electronics working with high-T_c SQUIDs in open space *J. Commun. Technol. Electron.* **53** 1259

[51] Schwarz T, Nagel J, Wölbing R, Kemmler M, Kleiner R and Koelle D 2013 Low-noise nano superconducting quantum interference device operating in tesla magnetic fields *ACS Nano* **7** 844

[52] Schwarz T, Wölbing R, Reiche C F, Müller B, Martínez-Pérez M J, Mühl T, Büchner B, Kleiner R and Koelle D 2015 Low-noise $YBa_2Cu_3O_7$ nano-SQUIDs for performing magnetization-reversal measurements on magnetic nanoparticles *Phys. Rev. Appl.* **3** 044011

[53] Faley M I, Poppe U, Urban K, Yu Slobodchikov V, Maslennikov Y V, Gapelyuk A, Sawitzki B and Schirdewan A 2002 Operation of high-temperature superconductor magnetometer with submicrometer bicrystal junctions *Appl. Phys. Lett.* **81** 2406

[54] Dammers J, Chocholacs H, Eich E, Boers F, Faley M, Dunin-Borkowski R E and Shah N J 2014 Source localization of brain activity using helium-free interferometer *Appl. Phys. Lett.* **104** 213705

[55] Öisjöen F, Schneiderman J F, Astalan A P, Kalabukhov A, Johansson C and Winkler D 2010 A new approach for bioassays based on frequency-and time-domain measurements of magnetic nanoparticles *Biosens. Bioelectron.* **25** 1008

[56] Global Status Report on Noncommunicable Diseases 2010 Geneva, Switzerland: World Health Organization http://who.int/nmh/publications/ ncd_report_full_en.pdf (Accessed: 4 February 2017)

[57] Chaikovsky I, Kohler J, Hecker T, Hailer B, Auth-Eisernitz S, Sosnytsky V, Feinzilberg L, Budnik N and Steinberg F 2001 Detection of coronary artery disease in patients with normal or unspecifically changed ECG on the basis of magnetocardiography *Biomag 2000: Proc. 12th Int. Conf. on Biomagnetism (Espoo, Finland, 13–17 August 2000)* ed J Nenonen *et al* (Helsinki University of Technology) p 565

[58] Yingmei L, Zaiqian C, Weiwei Q, Rong Y, Yue S, Zongjun L, Weiqing W, Huigen J and Guoping L 2015 Diagnostic outcomes of magnetocardiography in patients with coronary artery disease *Int. J. Clin. Exp. Med.* **8** 2441

[59] Maslennikov Y V *et al* 2012 The DC-SQUID-based magnetocardiographic systems for clinical use *Phys. Proc.* **36** 88

[60] Olesen J *et al* 2012 The economic cost of brain disorders in Europe *Eur. J. Neurol.* **19** 155

[61] Klem G H, Lüders H O, Jasper H H and Elger C 1999 The ten-twenty electrode system of the international federation. The international federation of clinical neurophysiology *Electroencephalogr. Clin. Neurophysiol.* **52** (Suppl.) 3

[62] Lypchuk T 1990 Dipole fit algorithms for MEG analysis. Magnes I/II system Software Reference Manual, (Biomagnetic Technologies, Inc., San Diego, CA)

[63] Dunin-Borkowski R E, McCartney M R, Frankel R B, Bazylinski D A, Pósfai M and Buseck P R 1998 Magnetic microstructure of magnetotactic bacteria by electron holography *Science* **282** 1868

[64] Kirschvink J L, Kobayashi-Kirschvink A and Woodford B J 1992 Magnetite biomineralization in the human brain *Proc. Natl Acad. Sci. USA* **89** 7683

[65] Chemla Y R, Grossman H L, Lee T S, Clarke J, Adamkiewicz M and Buchanan B B 1999 New study of bacterial motion: superconducting quantum interference device microscopy of magnetotactic bacteria *Biophys. J.* **76** 3323

[66] Tartaj P, del Morales M P, Veintemillas-Verdaguer S, Gonzalez-Carreno T and Serna C J 2003 The preparation of magnetic nanoparticles for applications in biomedicine *J. Phys. D: Appl. Phys.* **36** R182

[67] Veiseh O, Gunn J and Zhang M 2010 Design and fabrication of magnetic nanoparticles for targeted drug delivery and imaging *Adv. Drug. Deliv. Rev.* **62** 284

[68] Sensenig R, Sapir Y, MacDonald C, Cohen S and Polyak B 2012 Magnetic nanoparticle-based approaches to locally target therapy and enhance tissue regeneration *in vivo Nanomedicine* **7** 1425

[69] Enpuku K, Kuroda D, Yang T Q and Yoshinaga K 2003 High T_c SQUID system and magnetic marker for biological assays *IEEE Trans. Appl. Supercond.* **13** 371

[70] Yang C-C, Yang S-Y, Chieh J-J, Horng H-E, Hong C-Y, Yang H-C, Chen K H, Shih B Y, Chen T-F and Chiu M-J 2011 Biofunctionalized magnetic nanoparticles for specifically detecting biomarkers of Alzheimer's disease *in vitro ACS Chem. Neurosci.* **2** 500

[71] Yang S-Y, Chiu M-J, Lin C-H, Horng H-E, Yang C-C, Chieh J-J, Chen H-H and Liu B-H 2016 Development of an ultra-high sensitive immunoassay with plasma biomarker for differentiating Parkinson disease dementia from Parkinson disease using antibody functionalized magnetic nanoparticles *J. Nanobiotechnol.* **14** 1

[72] Bednorz J G and Müller K A 1986 Possible high T_c superconductivity in the Ba–La–Cu–O system *Z. Phys.* B **64** 189

[73] Zhang Y, Tavrin Y, Mück M, Braginski A I, Heiden C, Hampson S, Pantev C and Elbert T 1993 Magnetoencephalography using high temperature rf SQUIDs *Brain Topography* **5** 379

[74] Yokosawa K, Tsukamoto A, Suzuki D, Kandori A, Miyashita T, Ogata K, Seki Y and Tsukada K 2003 A 16-channel high-T_c SQUID-magnetometer system for magnetocardiogram mapping *Supercond. Sci. Technol.* **16** 1383

[75] Barthelmess H-J, Halverscheid M, Schiefenhovel B, Heim E, Schilling M and Zimmermann R 2001 Low-noise biomagnetic measurements with a multichannel dc-SQUID system at 77 K *IEEE Trans. Appl. Supercond.* **11** 657

[76] Kim I-S, Yu K K, Lee Y H, Kim K W and Park Y K 2005 High-T_c SQUID magnetometers for low noise measurements of magnetocardiograms *IEEE Trans. Appl. Supercond.* **15** 652

[77] Bechstein S, Kim I-S, Drung D, Novikov I and Schurig T 2010 Moderately shielded high-T_c SQUID system for rat MCG *J. Phys.: Conf. Ser.* **234** 042003

[78] Beyer J, Drung D, Ludwig F, Minotani T and Enpuku K 1998 Low-noise $YBa_2Cu_3O_{7-x}$ single layer dc superconducting quantum interference device (SQUID) magnetometer based on bicrystal junctions with 30° misorientation angle *Appl. Phys. Lett.* **72** 203

[79] Faley M I *et al* 2012 Magnetoencephalography using a multilayer high-T_c DC SQUID magnetometer *Phys. Proc.* **36** 66